Physics of Fluids

Stability of two-layer flows past slippery surfaces. II. Inclined channels

Cite as: Phys. Fluids **33**, 084113 (2021); https://doi.org/10.1063/5.0059217
Submitted: 07 June 2021 • Accepted: 28 July 2021 • Published Online: 27 August 2021

Himanshu Mishra, Anubhab Roy and S. Vengadesan

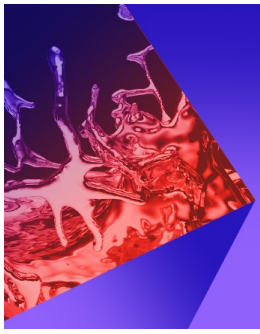

Physics of Fluids ARTICLE scitation.org/journal/phf

Stability of two-layer flows past slippery surfaces. II. Inclined channels

Cite as: Phys. Fluids 33, 084113 (2021); doi: 10.1063/5.0059217
Submitted: 7 June 2021 · Accepted: 28 July 2021 ·
Published Online: 27 August 2021

Himanshu Mishra,[1] Anubhab Roy,[1,a)] and S. Vengadesan[1,2]

AFFILIATIONS

[1]Department of Applied Mechanics, Indian Institute of Technology Madras, Chennai 600036, India
[2]Department of Mechanical Engineering, Virginia Tech., Blacksburg, Virginia 24061, USA

[a)]Author to whom correspondence should be addressed: anubhab@iitm.ac.in

ABSTRACT

In this paper, the linear stability characteristics of a two-layered liquid–liquid flow in an inclined channel with slippery walls are investigated. Previous studies on two-layered inclined channel flows have observed the presence of multiple base state flow profiles, two for countercurrent flow and up to three base states for co-current flow. The role of wall slip on the multiple base states associated with each holdup solution is analyzed here. Subsequently, a linear stability analysis, using a combination of a long-wave asymptotic analysis and finite wavenumber numerical calculation, is carried out with the slip boundary condition. Neutral stability boundaries are presented for each base state, with comparisons made with the previous results obtained for the no-slip boundary condition. It was found that the wall slip could have both stabilizing and destabilizing effects depending on the flow rates and the value of holdup—the location of an interface.

I. INTRODUCTION

A layered flow occurs as a particular case of stratified flow when the fluid properties like viscosity and density undergo a jump across an interface. They find several industrial applications, such as in oil transportation, polymer reactors, and microfluidic devices. The layered flows are also common in various geophysical settings from the confluence of river systems Konsoer and Rhoads[1] to the long-lived formation of "staircases" in oceans, homogeneous layers of liquid undergoing sharp jumps in density (Ponetti *et al.*[2]).

A stability analysis of the layered flows is essential in identifying the operating parameters for transporting immiscible liquids and also advances the understanding of the physics of mixing and the transition to turbulence in stratified systems. Multi-layered shear flows (three or more layers) are prone to inviscid instabilities occurring due to the interactions of waves riding at the interfaces (Carpenter *et al.*[3]). In contrast, two-layered flows are susceptible to viscous instabilities, occurring due to the stratification in viscosity (Govindarajan and Sahu[4]). Yih,[5] in his pioneering study, did a long-wave analysis of two-layered immiscible Couette flow and showed that instability could develop in fluids even at a low Reynolds number. He identified this instability as an interfacial mode, arising due to the difference in the two fluids' viscosity. Later, Hooper and Boyd[6] attempted a short-wave analysis of unbounded two-layered co-current Couette flow with the same fluid density and concluded that the flow is always unstable with zero surface tension. They remarked that the surface tension always brings stability to the flow, unlike the density stratification, which could either stabilize or destabilize a flow. Yiantsios and Higgins[7] carried out an extensive asymptotic and numerical stability analysis of a two-layered horizontal channel flow, considering the role of parameters like thickness ratio, density difference, surface tension, and effect of gravity as well. They calculated the critical Reynolds number for the onset of both interfacial and shear modes of instability. Recently, Kaffel and Riaz[8] have done a detailed study of the eigenvalue spectrum of two-layered horizontal channel flow and evaluated the temporal growth rate for different parameters for both shears and interfacial modes. They observed coalescence of both modes in both stable and unstable parts.

A gravity-driven liquid layer, with a stress-free interface, flowing down an incline is unstable to long-wave disturbances (Yih[9] and Kalliadasis[10]). The deformed interface induces a perturbation shear stress proportional to the base-state velocity profile's curvature to enforce the zero stress boundary condition. The competition of the inertial stresses and the lubrication pressure leads to instability (Smith[11]). Smith[11] also identified another mechanism of instability when the free surface has a fixed tangential velocity boundary condition.

A horizontal two-layered channel flow has left–right symmetry, and thus, reversing the direction of the pressure gradient does not alter

the instabilities. Tilley *et al.*[12] pointed out the lack of left–right symmetry in the inclined problem, where the pressure gradient can act either with or opposite to gravity. Vempati *et al.*[13] carried out a linear stability analysis in two-layered inclined channel flows. They considered the effect of density and viscosity stratification, surface tension, and inclination angle on instability. Trifonov[14] considered the countercurrent gas–liquid inclined channel flows and demonstrated that unstable surface mode is significantly affected by the gas velocity, inclination angle, and the width of the channel.

In most of the studies mentioned above in the inclined two-layered flows, multiple holdup solutions were not considered while carrying out the stability analysis. Multiple holdups are the characteristics of gravity-driven inclined channel flows where multiple base states can exist for a fixed inclination and flow rate ratio. Landman,[15] and Barnea and Taitel[16] found that multiple solutions exist for air–water two-layered inclined flows. They showed that the lower holdup solution, where the liquid's height is shallower than the gas's height, is most stable. Experiments have been performed on liquid–liquid two-layered flows by Ullmann *et al.*[17] They have shown that two holdup solutions can exist in countercurrent flows, and three holdup solutions can exist in co-current flows for a certain range of flow rate ratios. Further, they showed that TP (two plate) model gives a better prediction of holdup solutions and is in good agreement with their experiments. Also, TF (two-fluid) model needs adjustment of its closure laws and provides a poor prediction of the holdup. Kushnir *et al.*,[18] carried out a linear stability analysis in a long-wave limit of a wavenumber k in a two-layered horizontal and inclined channel flow, considering all multiple holdup solutions for countercurrent and co-current flow. Barmak *et al.*,[19,20] extended their study to finite wavelength stability. They found that long-wave perturbations are the most critical for liquid–liquid countercurrent flow; however, for air–water countercurrent flows, finite and short-wave are the most critical perturbation in certain flow rates. An interesting feature of the backflow scenarios in the two-layered co-current flow has been studied by Thibault *et al.*[21] Picchi *et al.*[22] carried out a linear stability analysis in a two-layered shear thinning fluid in both the horizontal and inclined channels. They considered multiple base states in a two-layered inclined channel.

In recent years, many investigations into the slip boundary condition at the channel walls are being reported due to vital applications in the studies of the polymer melt, microfluidics, rarefied flows, and biological flows.[23–25] To characterize the effect of slip, the Navier slip boundary condition[26] is often used as a standard model. The modified boundary condition relates the wall tangential velocity to the shear rate at the surface, with the constant proportionality being referred to as the slip length. Miksis and Davis[27] studied the effect of surface coatings and roughness of walls on flows and derived a useful slip boundary condition. They stated that the slip coefficient's magnitude following the Navier slip boundary condition equals the average amplitude of roughness at walls for the minimal roughness amplitude. The experiments have been done on the liquid film flowing over a hydrophobic wall in nano- and microchannels (Watanabe *et al.*,[28–30] Pit *et al.*,[31] Tretheway and Meinhart,[24] Ruckenstein and Rajora[32]). They found that modeling a fluid flow with a Navier slip condition would be more accurate in hydrophobic channel walls. Tretheway and Meinhart[24] measured velocity profile of water on 30 × 300 μm microchannel with a wall coating of 2.3 nm thick monolayer of octadecyl trichlorosilane (OTS). They observed a slip length of 1 μm with 10% of a velocity slip. Further, the slip length obtained from the experiments are varied as 0.05–0.4 (Tretheway,[24] Watanabe *et al.*,[30] Churaev *et al.*,[33] and Ichikawa *et al.*[34]). Other experiments reported even larger values of slip length up to thousand micrometers (Migler *et al.*,[35] Mhetar and Archer,[36] and Lee *et al.*[37]). Voronov *et al.*[38] studied the slip length associated with different rough surfaces and studied the dependence of contact angle and slip length. Recently, Liu and Zhang[39] carried out the numerical simulations on flat plate boundary layers with the superhydrophobic wall. They concluded that wall slip brings delay in the natural transition. Recently, a detailed comprehensive review study on slippery surfaces has been done by Samaha and Gad-el Hak[40].

The Navier slip boundary condition is often used to model flow past porous surfaces, with the slip length being proportional to the permeability of the porous medium.[41] Pascal[42] carried out a long-wave stability analysis of a gravity-driven flow down a porous inclined surface and showed that increasing the permeability (alternatively slip length) can destabilize the flow flowing above the porous substrate. Ghosh and Usha,[43] studied the stability of two-layered miscible liquid, flowing down in an inclined channel with a wall slip. They found stability at a higher Reynolds number in an overlap region when the interface is not near the slippery wall. Several studies have been done in one- and two-layered (miscible) channel flows with both horizontal and an inclined channel configurations.[4,44–51] In most of these studies, slip plays a dual role in stabilizing and destabilizing a flow. Lauga and Cossu[23] carried out the non-modal analysis and have shown a weak dependence of slip boundary conditions on transient energy growth. They further reported a higher value of critical Reynolds number in a shear mode. Min and Kim[52] studied the effects of wall slip in a shear flow on stability and transition. They showed that stream-wise wall slip delays the transition to turbulence, and spanwise wall slip is responsible for early transition in turbulence. Further, Samanta[53] has also carried out an investigation into the effect of slip velocity on the non-modal transient growth. Recently, an absolute or convective stability analysis in diffusive two-layer flow with wall slips was carried out.[54–56] The stability of such a system depends on the location of the diffusive layer from the slippery walls. Also, the dynamical studies have been performed to explain the instability in the Couette–Poiseuille flow.[57] The authors have explained the stabilizing effects on flow by moving the top plate via non-modal analysis. Further lately, Chakraborty *et al.*[58] have studied the hydrodynamic instability of non-Newtonian free surface flow down the inclined plane with the slippery wall and demonstrated that a slip could promote the onset of the instability in the flow. They have demonstrated that the long-wave perturbations are the most unstable ones on increasing the slip parameter. This paper investigates the influence of wall slip in two layers of immiscible fluids flowing in an inclined channel. We investigate the role of slip on the multiple holdup solutions and their subsequent linear stability. We have also carried out a complementary investigation on the stability of two-layer flow in slippery horizontal channels in Paper I.[59] The results of this work can be found in the paper of Ramakrishnan *et al.*[59]

The paper is organized as follows: First, we discuss the problem formulation with the governing conservation equations and boundary, and the geometry of a problem, and the governing equation is given in Sec. II. Base state calculations with multiple holdup solutions and wall

slip boundary conditions presented in Sec. III. A linear stability analysis is done using an asymptotic expansion in a long-wave limit in Sec. IV followed by a finite wavenumber numerical calculation in Sec. V.

II. FORMULATION OF PROBLEM

In this paper, an immiscible and incompressible two-layered fluid in an inclined channel is considered, as shown in Fig. 1 ($0 \le \theta \le \frac{\pi}{2}$). The bottom and upper layers of fluid are labeled as $j = 1, 2$, respectively. The flow is assumed to be two-dimensional, driven by the combined effects of gravity and pressure gradient in the x-direction. Using the depth of top layer h_2 as the length scale and the interfacial velocity U_I as the velocity scale, the following non-dimensional governing equations are derived as

$$\nabla.\mathbf{u}_j = 0, \tag{1}$$

$$\frac{\partial \mathbf{u}_j}{\partial t} + \mathbf{u}_j.\nabla\mathbf{u}_j = -\frac{\rho_1}{r\rho_j}\nabla p_j + \frac{1}{Re_2}\frac{\upsilon_j}{\upsilon_2}\nabla^2\mathbf{u}_j + \frac{\hat{\mathbf{g}}}{Fr_2}, \tag{2}$$

where $(u_j,\ v_j)$ is the fluid velocity of the layer $j(=1,2)$ and $\hat{\mathbf{g}} = (\sin\theta, -\cos\theta)$. The lower and upper flows are bounded by $-n < y < 0$ and $0 < y < 1$ region, respectively, $n = h_1/h_2$ being the depth ratio. The relevant non-dimensional parameters are the Reynolds number and Froude number, defined for layer 2 as $Re_2 = \frac{\rho_2 U_I h_2}{\mu_2}$ and $Fr_2 = \frac{U_I^2}{gh_2}$.

Here, μ_j, υ_j, and ρ_j are the dynamic viscosity, kinematic viscosity, and density of layer j, respectively (Table I).

The Navier[26] slip boundary condition has been used to model the slippery walls. The Navier slip boundary condition assumes that flow velocity u at solid walls is directly proportional to the shear stress at the surface

$$\mathbf{u} = \mathbf{U_w} + \lambda(\boldsymbol{\delta} - \mathbf{nn}).(\mathbf{E}.\mathbf{n}),$$

where $\boldsymbol{\delta}$ is the rank 2 identity tensor, E is the strain rate tensor, $\mathbf{n}$ is the unit normal vector from the surface to fluid, λ is the slip length, and $\mathbf{U_w}$ is the velocity at walls. If β is the non-dimensional slip length defined as $\beta = \frac{\lambda}{h_2}$, then the slip boundary conditions become $(\mathbf{U_w} = 0)$, at the bottom wall $y = -n$

$$\mathbf{u_1} = \beta\frac{\partial \mathbf{u_1}}{\partial y}, \tag{3}$$

and at the top wall $y = 1$

$$\mathbf{u_2} = -\beta\frac{\partial \mathbf{u_2}}{\partial y}. \tag{4}$$

Many experiments have been done in the past to determine the relevant slip lengths to be considered. Lumma *et al.*[60] had conducted an experiment based on the double-focused fluorescence cross correlation and determined the slip length obtained. They revealed a slip length of 1 μm in the 100 μm channel height, corresponding to a non-dimensional slip of $\beta = 0.1$. Boehnke *et al.*[61] had conducted the sedimentation experiments, and by using a scanning force microscope (SFM) for a force measurement revealed a slip length of $O(0.1)$. Lauga *et al.*[62] presented a detailed review of slip boundary conditions and measured a slip length in the slippery walls. This allows us to consider higher non-dimensional slip length up to $O(0.1)$. The experiments that have been done on the boundary layer flow over a porous flat plate reveal that wall slip depends on the characteristic β (non-dimensionalized by displacement thickness) that can cross the value of 0.1 and a porosity.[63,64] Lu *et al.*[65] showed that an effective smooth surface could replace fibrous porous by using tensorial Navier-slip boundary condition. Through numerical simulation, slip lengths ($\beta > 0.1$) are characterized as a function of porosity, channel height, and volume fraction. In this paper, we explore different stability properties of fluid with $\beta = 0.05$ and 0.1.

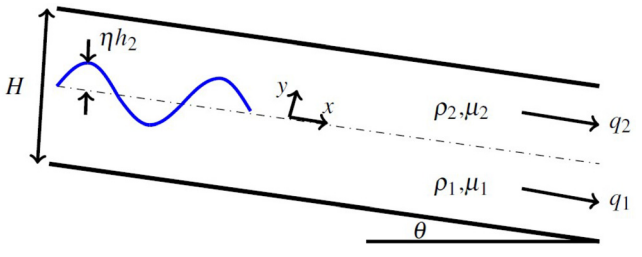

FIG. 1. Schematic diagram for a two-layered inclined channel flow (perturbation amplitudes are not to scale).

TABLE I. Parameters used in this paper.

Parameters	Definitions
μ_1, μ_2	Dynamic viscosity of fluid 1 and 2, respectively
ρ_1, ρ_2	Density of fluid 1 and 2, respectively
q_1, q_2	Flow rates of fluid 1 and 2, respectively
$m = \mu_1/\mu_2$	Viscosity ratio
$n = h_1/h_2$	Depth ratio
$r = \rho_1/\rho_2$	Density ratio
β	Non-dimensional slip coefficient
q_j	Flow rate of jth layer
u_i	Interfacial velocity
γ	Interfacial surface tension co-efficient
λ	Dimensional slip length

At the liquid–liquid interface $y = \eta(x,t)$, flow velocities of both layers and tangential stresses are continuous across the interface. Surface tension provides a jump to the normal stresses at the interface. The boundary conditions at the interface are

$$\mathbf{u_1} = \mathbf{u_2}, \tag{5a}$$

$$v_j = \frac{\partial \eta}{\partial t} + u_j\frac{\partial \eta}{\partial x}, \tag{5b}$$

$$[\mathbf{t}\cdot\mathbf{T}\cdot\mathbf{n}] = \left\{\frac{m\mu}{\mu_1}\left(\left(\frac{\partial u}{\partial y} + \frac{\partial v}{\partial x}\right)\left(1 - \left(\frac{\partial \eta}{\partial x}\right)^2\right) - 4\frac{\partial u}{\partial x}\frac{\partial \eta}{\partial x}\right)\right\} = 0, \tag{5c}$$

$$[\mathbf{n}\cdot\mathbf{T}\cdot\mathbf{n}] = \left[p + \frac{m\mu}{\mu_1}\left(\frac{Re_2^{-1}}{1 - (\partial\eta/\partial x)^2}\right)\frac{\partial u}{\partial x}\left(1 - \left(\frac{\partial \eta}{\partial x}\right)^2\right) + \left(\frac{\partial u}{\partial y} + \frac{\partial v}{\partial x}\right)\frac{\partial \eta}{\partial x}\right] = \frac{We_2^{-1}\left(\partial^2\eta/\partial x^2\right)}{\left(1 + (\partial\eta/\partial x)^2\right)^{3/2}}, \tag{5d}$$

where $[\cdot]$ denotes jump of quantity across the interface. $\mathbf{T}$ denotes the stress tensor, $\mathbf{n}$ is the normal unit vector from bottom fluid to top fluid, and $\mathbf{t}$ is the unit tangent vector to the interface. The non-dimensional Weber number is defined as $We_2 = \frac{\rho_2 h_2 U_I^2}{\gamma}$.

III. THE BASE FLOW

A. Multiple holdup solution

The base state is considered as a fully developed, unidirectional parallel flow $\mathbf{u}_j = u_j(y)\hat{\mathbf{x}}$ in each layer. On solving the governing momentum equations and applying the boundary conditions, the base state velocity profiles in both layers are obtained as

$$u_j = 1 + a_j y + b_j y^2. \tag{6}$$

The coefficients from above velocity profile are as follows:

$$a_2 = m a_1, \tag{7a}$$

$$a_1 = \frac{(m + 2\beta(m-n) - n^2 + (1+2\beta)(n+2\beta)\bar{Y})}{(m((n+\beta)^2 + \beta(1+\beta)(2n+1) + n(n\beta+1)))}, \tag{7b}$$

$$b_1 = -\frac{n((n+\beta) + m(1+\beta)) - (n+\beta)(1+2\beta)\bar{Y}}{nm((n+\beta)^2 + \beta(1+\beta)(2n+1) + n(n\beta+1))}, \tag{7c}$$

$$b_2 = -\frac{m(1+\beta) + n + \beta + (1+\beta)(n+2\beta)\bar{Y}}{(n+\beta)^2 + \beta(1+\beta)(2n+1) + n(n\beta+1)}. \tag{7d}$$

The non-dimensional inclination parameter is given as

$$\bar{Y} = \frac{n(1-r)Re_2 \sin\theta}{2Fr_2}. \tag{7e}$$

Taitel and Dukler[66] have shown that the heavy phase layer thickness is a function of two non-dimensional parameters—the Lockhart Martinelli parameter and the inclination parameter Y. The Lockhart Martinelli parameter is defined as

$$X^2 = \frac{(-dP/dx)_{1S}}{(-dP/dx)_{2S}} = m.q, \tag{8}$$

where $q = q_1/q_2$ is the flow rate ratio. The positive flow rate ratio q is obtained in the co-current flow. Hence, the co-current flow regime satisfies $X^2 > 0$. Similarly, in countercurrent flows, the flow rates are opposite and satisfy $X^2 < 0$. The inclination parameter is defined as

$$Y = \frac{(\rho_1 - \rho_2)g\sin\theta}{(-dP/dx)_{2s}}, \tag{9}$$

where the superficial pressure drop can be written as $(-dP/dx)_{js} = 12\mu_j q_j/H^3$. $H = h_1 + h_2$ is the total height of the channel. For density ratio $r > 1$, Y can determine the top layer's flow direction. When $Y < 0$, then the top layer is flowing in the upward direction (against gravity); similarly when $Y > 0$, then the top layer is flowing in a downward direction. Holdup h is an important parameter in the multiphase flow, used for determining a base state. It can be defined as a portion of a certain fluid occupied in a channel, $h = h_1/H = n/(n+1)$. The superficial velocity is defined as $U_{js} = q_j/H$.

Mass conservation equations are given as

$$\int_{-h}^{0} \frac{\hat{u}_1}{U_{1s}} d\bar{y} = 1, \tag{10a}$$

$$\int_{0}^{1-h} \frac{\hat{u}_2}{U_{2s}} d\bar{y} = 1, \tag{10b}$$

where $\bar{y} = y/H$. Then inclination parameter can be obtained as a function of holdup h, m, X^2, and slip coefficient β,

$$\begin{aligned} Y = &\frac{h^3(-4h\beta + h + 4\beta)}{4(h-1)^3h^2((h-1)(4\beta+1)m\xi_1 - h(3\beta+1)\xi_2)} \\ &+ \frac{(h-1)hm\left(12(h-1)\beta^2 + 2(h(4h-3)-3)\beta - h(h+3)\right)}{4(h-1)^3h^2((h-1)(4\beta+1)m\xi_1 - h(3\beta+1)\xi_2)} \\ &- \frac{(h-1)^2X^2\left(h^2\xi_3 - 2h(\beta(6\beta+4m-5)+m-2) + 4\beta\xi_4 + m\right)}{4(h-1)^3h^2((h-1)(4\beta+1)m\xi_1 - h(3\beta+1)\xi_2)}, \end{aligned} \tag{11}$$

where $\xi_1 = (3(h-1)\beta - h)$, $\xi_2 = (4(h-1)\beta - h)$, $\xi_3 = (4\beta(m-2) + m - 1)$, and $\xi_4 = (3\beta + m + 1)$.

The non-dimensional pressure drop is

$$\begin{aligned} \bar{P} = &\frac{h(4(h-1)(\beta+1)m\xi_1 + h(-4h\beta + h + 4\beta))}{4(h-1)^3h((h-1)(4\beta+1)m\xi_1 - h(3\beta+1)(4(h-1)\beta - h))} \\ &+ \frac{3(h-1)^2(2\beta+1)X^2(2(h-1)\beta - h)}{4(h-1)^3h((h-1)(4\beta+1)m\xi_1 - h(3\beta+1)(4(h-1)\beta - h))}. \end{aligned} \tag{12}$$

At the interface $y = \eta(x,t)$, the interfacial velocities, which are used to scale the eigenvalues and finding superficial Reynolds number Re_{js} as a function of Re_j, are given as

$$\frac{U_I}{U_{1s}} = -\frac{6(h-1)(h(\beta+1)Y(2(h-1)\beta - h) - \bar{P}(h+\beta)\xi_5)}{q((h-1)(\beta+1)m + h\beta - h - \beta)}, \tag{13a}$$

$$\frac{U_I}{U_{2s}} = -\frac{6(h-1)(h(\beta+1)Y(2(h-1)\beta - h) - \bar{P}(h+\beta)\xi_5)}{(h-1)(\beta+1)m + h\beta - h - \beta}. \tag{13b}$$

In the above equations, $\xi_5 = (2(h-1)\beta - 1)$. Note that $\bar{P}$ and u_i are expressed in terms of four non-dimensional parameters. From the above expressions, Y and $\bar{Y}$ can be related as

$$\bar{Y} = -6Y\left(\frac{U_{2s}}{U_I}\right)\left(\frac{n}{(n+1)^2}\right). \tag{14}$$

After solving, we get $\bar{Y}$ in terms of h, m, β, and Y as

$$\bar{Y} = -\frac{(h-1)^2hY\left(h^2(4\beta(m-2)+m-1) - 2h(\beta\xi_6 + m - 2) + 4\beta(3\beta+m+1) + m\right)}{-2h^2\beta - 2h\beta^2 + h(h-1)^3(4\beta+1)Y(2(h-1)\beta - h) + 2h\beta + h + 2\beta^2 + \beta}, \tag{15}$$

where $\xi_6 = (6\beta + 4m - 5)$.

Multiple holdup solutions are the characteristic property of the inclined two-layered channel flows. Earlier, it was reported that two holdup solutions are associated with countercurrent inclined flow, and three holdup solutions can be obtained in co-current flow regime.[17] Multiple base states can be obtained at different ranges of flow rate ratios by fixing viscosity ratio m and inclination parameter Y from Eq. (11) (see Fig. 2). When $Y = 0$, the flow is driven by the pressure gradient only. Non-zero Y corresponds to a situation where gravity effects, along with a pressure gradient, are responsible for flow in a channel. The triple solutions are obtained at a higher X^2 in downward co-current flows. Similarly, in upward co-current flow, the triple solutions region is obtained at a lower range of X^2, which is shown in Fig. 2(b).

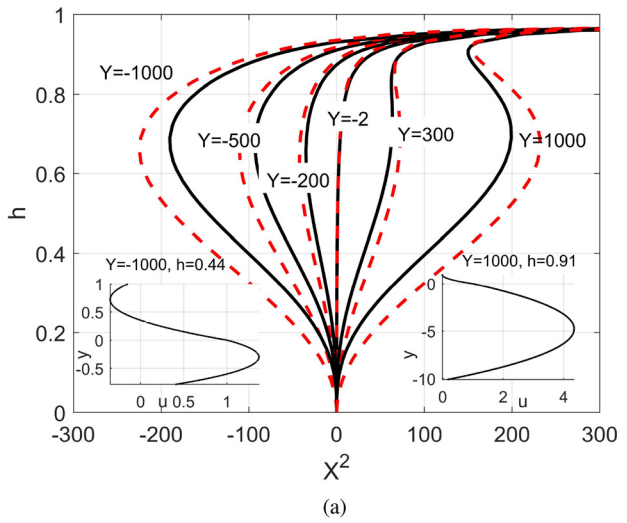

(a)

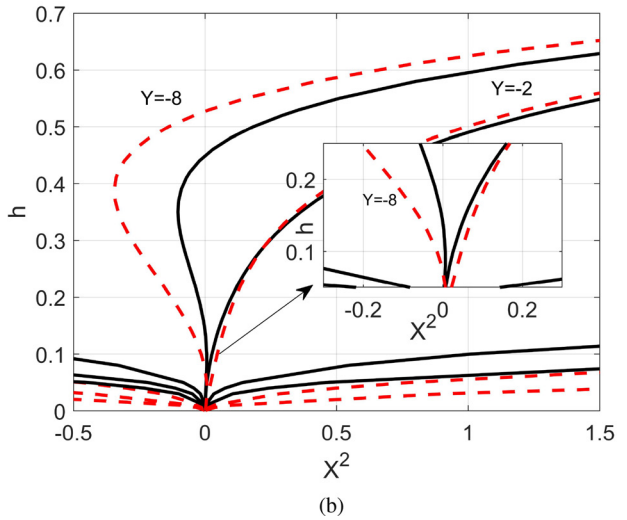

(b)

FIG. 2. Multiple holdup solutions as a function of X^2 when $m = 1.52$. In (a), single, double, and triple holdup solutions with different Y are shown; in (b), triple holdup solution in upward co-current flow is shown when $Y = -8$. The solid black line corresponds to the no-slip condition, and the red dashed line corresponds to the wall slip condition when $\beta = 0.1$.

Equation (11) plays a significant role in determining multiple base states at a fixed flow rate ratio in both countercurrent and co-current flows. No solution is obtained in countercurrent flow with slip, where the top layer flows in a downward direction ($X^2 < 0$, $Y > 0$). Since holdup h depends on q, moving a location of an interface from the bottom to the top wall, the direction of flow can be changed, as shown in Fig. 2. The countercurrent region converts to a co-current region at higher holdups. Similarly, the upward co-current flow converts into a countercurrent regime for a small range of flow rate ratios q. The variations of flow rate ratio q with holdups at different inclination parameters and non-dimensional wall slip coefficient $\beta = 0.1$ are shown in red curves (see Fig. 2). The holdup in an entire curve is divided into lower holdups (where all holdup values in a solution lie below the local maxima) and higher holdups solutions in a countercurrent flow regime. The flooding is a higher limit in terms of flow rates until the base state of the two-layer configuration can be obtained. The flooding point is located where the lower and higher solutions merge and occupy each base state curve's local maxima. Beyond the flooding point, no holdup solutions for any Y will be obtained in countercurrent flows.

With wall slip $\beta = 0.1$, base states are obtained at a higher range of flow rate ratio in the lower holdup region of the curve. However, the location of a liquid interface is almost the same. It can be interpreted in two ways: either the bottom layer flow rate increases or the top layer flow rate decreases. At the higher holdup region of the curve, the base state is obtained at almost the same flow rate ratio as the no-slip condition but at a higher holdup value (the interface obtained is closer to the top wall). However, the effect of the wall slip on the base state at higher holdup is minimal. Moreover, when the flow is driven by pressure gradient ($Y \approx 0$), the wall slip only influences the base state at higher holdups. At lower holdups, the difference between the flow rate ratio obtained with and without slip seems to increase at the higher values of Y in both countercurrent and co-current flows.

Interestingly, the transition from single- to triple-solution region is expected to be obtained at the relatively low values of Y with wall slip boundary conditions. The velocity profiles have been shown in countercurrent region and upward co-current flow (see Fig. 2). At $Y \neq 0$, wall slips help gravity span multiple base states to a higher range of q in both countercurrent and co-current flows.

In Fig. 3, the surface plot of the holdup as a function of X^2 and Y with $m = 1.52$ and $\beta = 0.1$ is shown. Gray patches correspond to the

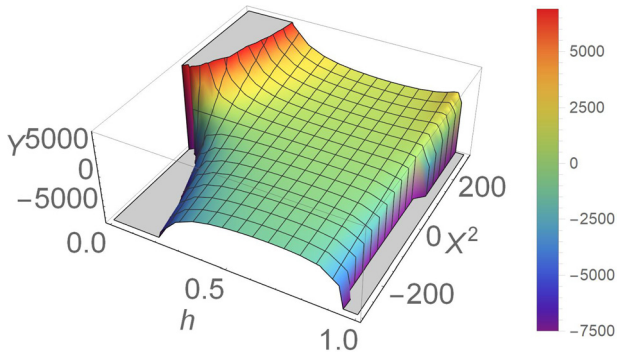

FIG. 3. 3D holdup surface plot as a function of X^2 and Y with $m = 1.52$ and $\beta = 0.1$.

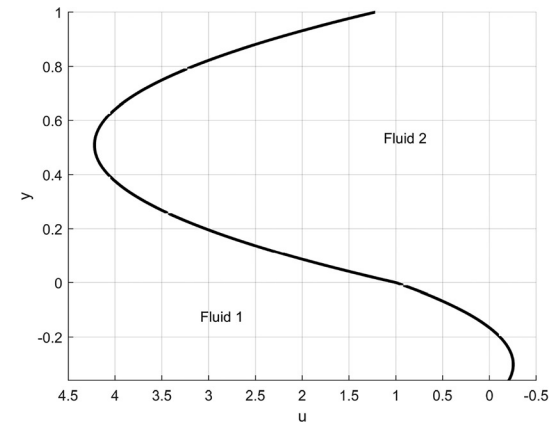

(a)

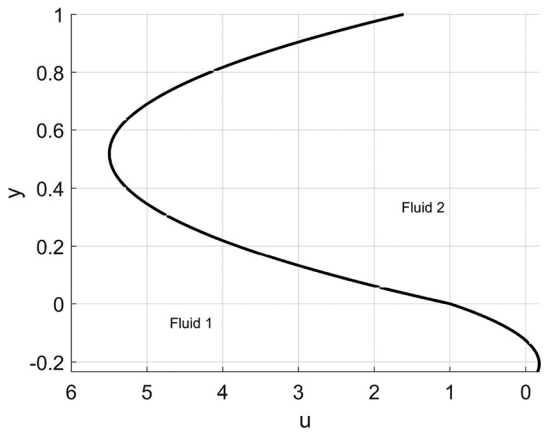

(b)

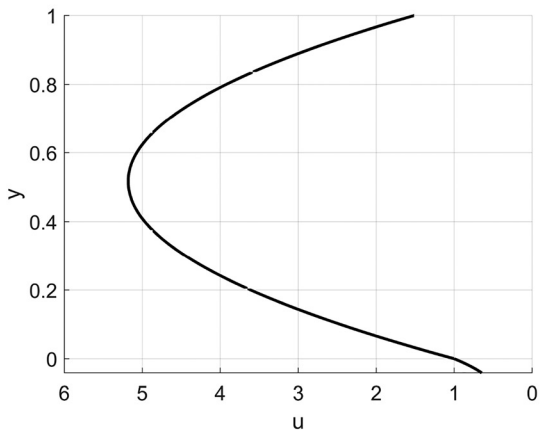

(c)

FIG. 4. Velocity profiles with different holdup h [for marked points see Fig. 6(b)], (a) $h = 0.27$, marked with point A, (b) $h = 0.19$, marked with point B and (c) $h = 0.04$, marked with point C. Also, $Y = -4.5$ and $\beta = 0.1$.

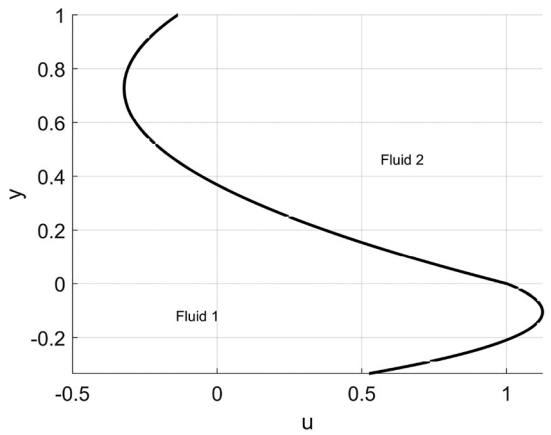

(a)

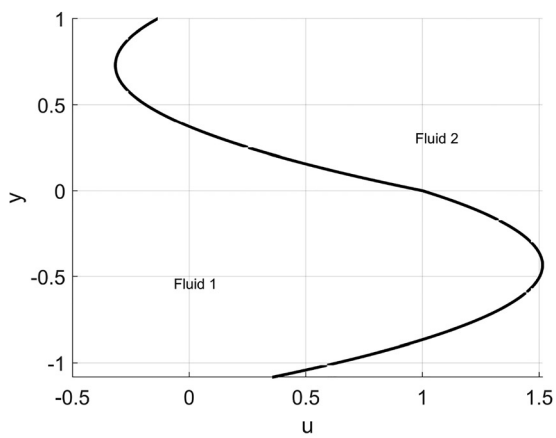

(b)

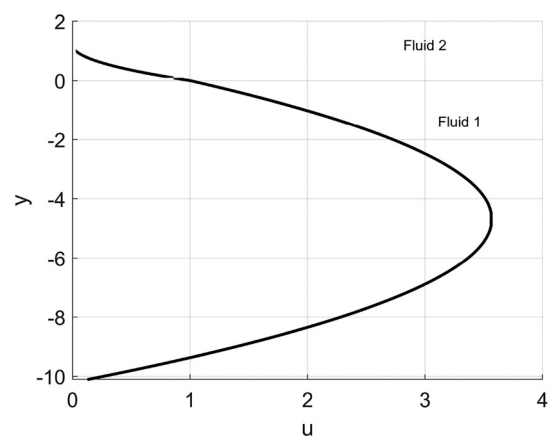

(c)

FIG. 5. Velocity profiles with different holdup h [for marked points see Fig. 6(b)], (a) $h = 0.25$, marked with point D, (b) $h = 0.52$, marked with point E and (c) $h = 0.91$, marked with point F. Also, $Y = 500$ and $\beta = 0.1$.

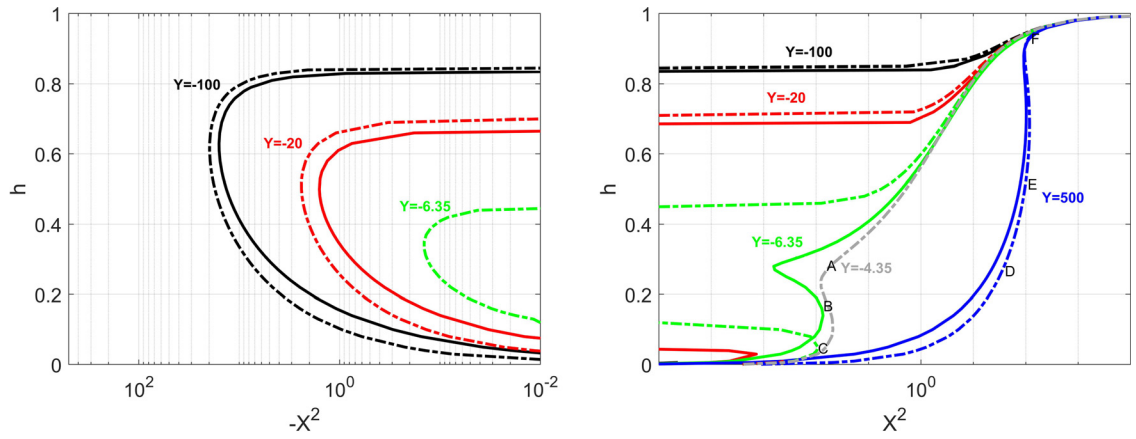

FIG. 6. Plot of h vs X^2 for $m = 1.52$ in (a) countercurrent regime and in (b) co-current regime. Dashed lines represent the slip boundary condition $\beta = 0.1$, whereas the solid lines are indicating the no slip boundary condition with the same Y.

no solution region. Two such patches are shown at lower holdup for all X^2 except close to zero. Another gray patch is shown at higher holdups where the holdup solution is getting closer to unity (when Y is constant in Fig. 2). Moreover, the interface obtained closer to the top wall in co-current flow comparatively. The countercurrent ($X^2 < 0$) and co-current ($X^2 > 0$) regions are distinguishable, where the surfaces are curved upward (or downward) at $X^2 = 0$. The triple solution is visible at a higher h, and positive X^2 pointed outward.

This paper's main objective is to study the linear stability in a two-layered inclined channel flow considering multiple holdup solutions with wall slip. However, a local backflow is linked with the multiple holdup solutions depending on the flow direction in the co-current regime.

A local backflow is a phenomenon when a few layers of the flow near the wall reverse their direction. However, the net flow rate obtained in the flow still has the same sign. Recently, a detailed analysis has been done by Thibault *et al.*[21] using catastrophe theory and the principle of minimization of dissipation approach. In downward co-current flows ($Y > 0$), higher and intermediate holdups are characterized by the local backflow situation, and lower holdups are characterized by the local backflow in the upward co-current flow ($Y < 0$). The velocity profiles for both upward and downward co-current flows with backflow are shown in Figs. 4 and 5. Holdup curves for both countercurrent and co-current flows at logarithmic scale are shown in Fig. 6. The selection of holdups is considered for the velocity-profiles as mentioned above, taken from a Fig. 6(b).

IV. LINEAR STABILITY ANALYSIS

In this section, we study the evolution of two-dimensional infinitesimal perturbations in a two-layered inclined channel. Hesla *et al.*[67] demonstrated that two-dimensional disturbances are the most unstable ones, and Squire's theorem holds at least for horizontal stratified flows. Barmak *et al.*[68] demonstrated that Squire's transformation for a two-layered inclined channel requires additional constraints to inclination angle and flow rates of both the layers. However, they have demonstrated that the 2D perturbations are still the most critical ones than the 3D perturbations in the inclined channel flows. The parameters like velocities and pressure field are split into two parts, the base state and the perturbed quantity, which are given by $u_j = U_j + u'_j$, $v_j = v'_j$, $p_j = P_j + p'_j$, and $\eta = \eta'$.

These perturbed velocities defined in terms of their corresponding stream function as

$$u' = \frac{\partial \psi}{\partial y}, \quad v' = -\frac{\partial \psi}{\partial x}.$$

These perturbed quantities are substituted in governing equations and boundary conditions to get the perturbed momentum equations for both layers and boundary conditions. We express all perturbation quantities in terms of normal modes

$$\psi = \phi(y)e^{ik(x-ct)},$$
$$p' = \hat{P}(y)e^{ik(x-ct)},$$
$$\eta = H_\eta e^{ik(x-ct)},$$

where ϕ, $\hat{P}$, and H_η are the perturbation amplitudes in stream-function, pressure, and at interface, respectively.

In this paper, we focused on the temporal growth of perturbation in the long-wave regime. The non-dimensional wavenumber is represented by k ($k = \frac{2\pi h_2}{l_w}$, where l_w is a wavelength) whereas c is the non-dimensional complex wave speed ($c = c_r + ic_i$). c_r is the phase speed of the perturbation and kc_i is a growth rate of perturbation. The system is neutrally stable when $c_i = 0$.

We have used the interfacial velocity U_I for velocity and time scales. Since U_I can attain negative values, $c_i > 0$ can denote an instability when $U_I > 0$ and stability when $U_I < 0$.

Substituting the above-mentioned normal mode form in perturbed momentum equations, we get Orr–Sommerfeld equations for layer 1

$$\phi_1^{iv} - 2k^2\phi_1'' + k^4\phi_1 = ikRe_2 rm^{-1}\left[(U_1 - c)(\phi_1'' - k^2\phi_1) - \phi_1 U_1''\right], \tag{16}$$

and for layer 2

$$\phi_2^{iv} - 2k^2\phi_2'' + k^4\phi_2 = ikRe_2\left[(U_2 - c)(\phi_2'' - k^2\phi_2) - \phi_2 U_2''\right]. \tag{17}$$

The boundary condition in terms of the normal modes are given by
(a) Slip boundary condition at $y = -n$ is

$$\phi_1' = \beta\phi_1'', \tag{18a}$$

and at $y = 1$ is

$$\phi_2' = -\beta\phi_2''. \tag{18b}$$

(b) No-penetration boundary condition at $y = -n$ is

$$\phi_1 = 0, \tag{19a}$$

and at $y = 1$ is

$$\phi_2 = 0. \tag{19b}$$

(c) Continuity of the stream function at the interface $y = 0$

$$\phi_1 = \phi_2. \tag{20}$$

(d) Kinematic boundary condition at the interface $y = 0$

$$\phi_1' + \frac{\phi_1}{(c-1)}U_1' = \phi_2' + \frac{\phi_2}{(c-1)}U_2'. \tag{21}$$

(e) Tangential stress boundary condition at the interface $y = 0$

$$\phi_2'' + k^2\phi_2 + U_2''\frac{\phi_2}{(c-1)} = m\left(\phi_1'' + k^2\phi_1 + U_1''\frac{\phi_1}{(c-1)}\right). \tag{22}$$

(f) Normal stress boundary condition at the interface $y = 0$

$$\begin{aligned} &m(\phi_1''' - 3k^2\phi_1') - (\phi_2''' - 3k^2\phi_2') \\ &\quad + ikRe_2\left[r((c-1)\phi_1' + U_1'\phi_1) - ((c-1)\phi_2' + U_2'\phi_2)\right] \\ &= ikRe_2\left[(r-1)Fr_2^{-1}\cos\theta + k^2We_2^{-1}\right]\frac{\phi_2}{c-1}. \end{aligned} \tag{23}$$

Here, the prime ($'$) in a governing equation and boundary condition denotes differentiation with respect to y.

A. Long-wave asymptotic solution ($k \ll 1$)

Viscosity and density stratification can cause instability in the parallel flows.[69] Yih[5] studied the interfacial instability by using the long-wave analysis. In the long-wave asymptotics, the wavelength is assumed to be large compared to a channel height ($k \ll 1$). Eigenfunctions and eigenvalues are usually represented as a regular perturbation series given by

$$\phi_j = \phi_{j,0} + k\phi_{j,1} + k^2\phi_{j,2} + k^3\phi_{j,3} + \cdots, \tag{24a}$$

$$c = c_0 + kc_1 + k^2c_2 + k^3c_3 + \cdots. \tag{24b}$$

The expansions from Eqs. (24a) and (24b) are substituted in the Orr–Sommerfeld equations and the boundary conditions. We began by substituting the zeroth-order expressions ($\phi_{j,0}$ and c_0) in the above governing equations and boundary conditions. All terms which are coupled with k and its higher-order are neglected. The resulting equations thus obtained are termed as the zeroth-order Orr–Sommerfeld equations and boundary conditions. This procedure will be followed by substituting nth order terms ($\phi_{j,n}$ and c_n) in the governing equations to obtain the subsequent nth order Orr–Sommerfeld equations with the nth order boundary conditions. By solving these equations, eigenvalues expressions are sequentially determined at each order. We followed Higgins[7] and Kushnir *et al.*[18] and carried out a long-wave analysis in a two-layered flow inclined channel.

For zeroth-order approximation, ignoring all terms coupled with k in Orr–Sommerfeld equations and boundary conditions, we get

$$\phi_{j,0}^{iv} = 0,$$

where $j = 1, 2$.

Zeroth-order boundary conditions are

$$\begin{aligned} \phi_{1,0}' &= \beta\phi_{1,0}'' \quad \text{at } y = -n, \\ \phi_{2,0}' &= -\beta\phi_{2,0}'' \quad \text{at } y = 1, \\ \phi_{1,0} &= 0 \quad \text{at } y = -n, \\ \phi_{2,0} &= 0 \quad \text{at } y = 1. \end{aligned}$$

Zeroth-order interfacial boundary conditions at $y = 0$ are given as

$$\phi_{1,0}' + \frac{\phi_{1,0}}{(c_0-1)}U_1' = \phi_{2,0}' + \frac{\phi_{2,0}}{(c_0-1)}U_2', \tag{25}$$

$$\phi_{2,0}'' + U_2''\frac{\phi_{2,0}}{(c_0-1)} = m\left(\phi_{1,0}'' + U_1''\frac{\phi_{1,0}}{(c_0-1)}\right), \tag{26}$$

$$m\phi_{1,0}''' - \phi_{2,0}''' = 0. \tag{27}$$

Solutions of the zeroth-order governing equations, for fluid 1 is

$$\phi_{1,0} = c_0 - 1 + A_{1,0}^1 y + A_{1,0}^2 y^2 + A_{1,0}^3 y^3, \tag{28}$$

and for fluid 2 is

$$\phi_{2,0} = c_0 - 1 + A_{2,0}^1 y + A_{2,0}^2 y^2 + A_{2,0}^3 y^3. \tag{29}$$

In the above solutions, the superscripts in coefficients $A_{j,0}^n$ represent a numbering notation and should not be confused with an exponent. With assistance from boundary conditions, c_0 is obtained to be

$$\begin{aligned} c_0 = &\frac{8\beta^4(n+1)\left(2m(3n-1)\bar{Y} + 3m(n+1)^2 + 2(n-3)n\bar{Y}\right)}{(2\beta+n+1)(\beta n+\beta+n)\left(12\beta^2m(n+1)^2 + 4\beta\xi_7 + m^2 + 2m(n(2n+3)+2)n + n^4\right)} \\ &+ \frac{4\beta^3\left((n+1)\left(m^2(6n+2) + m(n+1)(n(5n+16)+5) + 2n^2(n+3)\right) + \bar{Y}\left(m(n(10n(n+2)-1)-3) + n(n(3n^2+n-20)-10)\right)\right)}{(2\beta+n+1)(\beta n+\beta+n)\left(12\beta^2m(n+1)^2 + 4\beta\xi_7 + m^2 + 2m(n(2n+3)+2)n + n^4\right)} \end{aligned}$$

$$+\frac{2\beta^2\left((n+1)\left(m^2(4n(n+4)+3)+2m(n(n(n(n+9)+25)+9)+1)+n^2\xi_{11}\right)+\bar{Y}\left(m\xi_{10}+n(n(n(n(n+7)-12)-24)-4)\right)\right)}{(2\beta+n+1)(\beta n+\beta+n)\left(12\beta^2m(n+1)^2+4\beta\xi_7+m^2+2m(n(2n+3)+2)n+n^4\right)}$$
$$+\frac{n(n+1)\left(m^2(2n+1)+mn(2n(n+\bar{Y}+3)-\bar{Y}+2)+n^2(n(n+\bar{Y}+2)-2\bar{Y})\right)}{(2\beta+n+1)(\beta n+\beta+n)\left(12\beta^2m(n+1)^2+4\beta\xi_7+m^2+2m(n(2n+3)+2)n+n^4\right)}$$
$$+\frac{\beta\left(m^2(n(n(8n+21)+12)+1)+mn(n(n(2n\xi_8+15\bar{Y}+64)-2\bar{Y}+34)-3\bar{Y}+4)+n^2(n(n(n\xi_9+2\bar{Y}+21)-15\bar{Y}+8)-8\bar{Y})\right)}{(2\beta+n+1)(\beta n+\beta+n)\left(12\beta^2m(n+1)^2+4\beta\xi_7+m^2+2m(n(2n+3)+2)n+n^4\right)}. \tag{30}$$

Here, $\xi_7 = m^2 + m(n+1)(n(n+5)+1) + n^3$, $\xi_8 = 2n + 4\bar{Y} + 17$, $\xi_9 = n + 3\bar{Y} + 12$, $\xi_{10} = (n(4n(n(n+6)+3)-7)-1)$, and $\xi_{11} = n(3n+16)+4$.

c_0 obtained is a real eigenvalue and is a function of n, m, and β. In the above equation, adding slip parameter significantly alters the expression of c_0. However, the real part of the wave speed cannot determine the instability. Note that $\beta = 0$ will result in the same expression as obtained by Kushnir *et al.*[18]

The first-order equations are derived by ignoring all $O(k^2)$ terms and collecting the $O(k)$ terms. These terms are then substituted in the governing equations and boundary conditions and solved together to obtain the first-order eigenvalue. The first-order stability equations are

$$\phi_{j,1}^{iv} = iRe_2\frac{\nu_2}{\nu_j}\left[(U_j - c_0)\phi_{j,0}'' - \phi_{j,0}U_j''\right]. \tag{31}$$

Here, the boundary conditions at the wall are the same as mentioned for zeroth-order equations. The interfacial boundary conditions ($y = 0$) evaluated until the first order of k are

$$c_1(\phi_{1,0}' - \phi_{2,0}') + (c_0 - 1)(\phi_{1,1}' - \phi_{2,1}') + \phi_{1,1}U_1' - \phi_{2,1}U_2' = 0, \tag{32a}$$

$$c_1(\phi_{2,0}'' - m\phi_{1,0}'') + (c_0 - 1)(\phi_{2,1}'' - m\phi_{1,1}'') = 0, \tag{32b}$$

$$m\phi_{1,1}''' - \phi_{2,1}''' + iRe_2(r(c_0-1)\phi_{2,0}' + U_2'\phi_{2,0}) - ((c_0-1)\phi_{1,0}' + U_1'\phi_{1,0}) - iRe_2\left(\frac{(r-1)\cos\theta}{Fr_2}\right)(\phi_{2,0}/(c_0-1)) = 0. \tag{32c}$$

The solutions of the first-order Orr–Sommerfeld equations are obtained as

$$\phi_{j,1} = iRe_2(A_{j,1}^1 + A_{j,1}^2y^2 + A_{j,1}^3y^3 + \zeta_j(y)), \tag{33}$$

where ζ_j is a particular integral. c_1 is an imaginary quantity and can be represented as a function of several parameters, $c_1 = f(m, n, \bar{Y}, \beta, \theta, Re_2, Fr_2, We_2, k, r)$. See attached supplementary material with this paper to get an expression for eigenvalues, and particular integral and other coefficients. The expression for c_1 is given as

$$c_1 = \frac{i(A_{2,1}^2Re_2(1-c_0) + A_{1,1}^2mRe_2(c_0-1))}{A_{2,0}^2 - A_{1,0}^2m}. \tag{34}$$

The first-order eigenvalue c_1 is used to find the neutral stability plots shown in Sec. V.

B. Numerical results

For arbitrary wavenumbers, the eigenvalue problem is solved numerically by using the Chebyshev collocation method. It discretizes Orr–Sommerfeld equations and gives the entire spectrum of eigenvalues and eigenfunctions for a given wavenumber. Previous studies on the stability of multiphase flows have focused on various applications like miscible fluids, non-Newtonian fluids, and flow in porous medium.[43,48,49]

The Orr–Sommerfeld equations are expanded in terms of Chebyshev polynomials. The Chebyshev polynomials are defined in a domain $[-1,1]$ unlike the natural domain of flow $[-n, 1]$. To convert into Chebyshev domain, we define, at $-n < y < 0$

$$z = \frac{2y+n}{n}, \tag{35}$$

and at $0 < y < 1$

$$z = 2y - 1. \tag{36}$$

The eigenfunctions are expressed as expansions of Chebyshev basis functions[70]

$$\phi_1^{(i)}(z) = \sum_{k=0}^{N_1} a_kT_k^{(i)}(y), \tag{37}$$

$$\phi_2^{(i)}(z) = \sum_{k=0}^{N_2} b_kT_k^{(i)}(y), \tag{38}$$

where i denotes the ith derivative with respect to y. T_k denotes the Chebyshev polynomials. a_k and b_k are unknowns and are discrete Chebyshev expansion coefficients. These expansions are put into governing equations and boundary conditions to obtain generalized eigenvalues problem in the form of

$$Ax = cBx.$$

The distribution of the number of grid points is non-uniform in spectral methods. The arrangement of grid points in a Chebyshev domain is defined as

$$z_j = \cos(\pi j/N). \tag{39}$$

More grid points are allocated near both the walls and interface. The variation of variables like velocity and vorticity are high and require fine grid structures to capture accurate solutions. The eigenvalue problem is solved by using MATLAB®, using a QZ algorithm.

V. RESULTS AND DISCUSSIONS

The instabilities in the shear flow of immiscible fluids can be divided into two modes. The shear flow instability is often observed at

TABLE II. Comparison between the present long-wave asymptotic results with the asymptotic results of Kushnir *et al.*,[18] with $m = 100$, $r = 2$, $\theta = 1$(rad), $We_2 = \frac{(1+n)Re_2^2}{25000}$, $k = \frac{0.001}{(1+n)}$.

n	Re_2	Fr_2	Kushnir *et al.*[18]	Present asymptotic (c_R, c_I)
0.5	5.0742	0.034 759	(0.296 938 43, 0.000 123 640 63)	(0.296 938 124 6, 0.000 123 641)
0.5	11.8	0.018 797	(0.691 813 25, 0.000 056 307 73)	(0.691 824 344 7, 0.000 056 305 99)
3	26.69	18.236	(6.118 395, 0.001 739 557 4)	(6.118 458 3, 0.001 739 585 5)
3	31.098	2.475 73	(5.215 411, 0.000 966 384)	(5.215 408 388, 0.000 966 389)

high Reynolds numbers for wall-bounded shear flows and could be responsible for the transition to turbulence. On the other hand, interfacial instabilities often develop at low Reynolds numbers. The long-wave analysis captures the interfacial mode of instabilities. The shear mode of instabilities is usually associated with a finite wavenumber analysis.[7]

The interface in a stratified flow can become unstable in several ways, viscosity and density stratification being possible causes. Barmak *et al.*[20] reported neutral stability plots in the long-wave and finite wave regime. They showed that the perturbations obtained in a long-wave limit are the most critical in liquid–liquid countercurrent flow stability. However, with air–water configuration, short-wave instabilities are more critical in a specific range of flow rates. We compared our analytical and numerical results with the results obtained by Kushnir *et al.*[18] (asymptotic results) and Tilley *et al.*[12] (numerical results) for an inclined channel flow with no-slip boundary condition. Eigenvalues are shown in Tables II and III. (c_R, c_I) are scaled by the characteristic velocity $\mu_1/\rho_1 H$.

Neutral stability curves have been shown for the two-layered inclined channel in the long-wave limit ($k \ll 1$), following Kushnir *et al.*,[18] with a wall slip boundary condition. Liquid properties are considered the same as mentioned in their work. It is known that the base state can be obtained when the flow rates lie in the region bounded by the flooding curve. However, the base states obtained in these regions can be unstable in both holdup solutions. Therefore, it is more convenient to show the neutral stability plots in terms of superficial velocities (or flow rates) to obtain the system's operational range in terms of flow rates. Wall slip can affect the stability at different ranges of flow rates. The range of these critical flow rates further depends on holdup solutions. With the slip boundary condition, we required at least four parameters to define a base state (Y, β, m and q). The instability in two-layered inclined channel flows with a multiple holdup solution can be determined by the seven non-dimensional parameters (Y, β m, X^2, r, θ, Re_{js}, or Fr_{js}). The superficial Reynolds number and Froude number can be defined as $Re_{js} = \rho_j U_{js} H/\mu_j$ and $Fr_{js} = U_{js}^2/gH$, respectively. In two-layered inclined flows, the density ratio is responsible for jump in a velocity curvature U_j'' resulting in extra component in the tangential stress boundary condition [see Eq. (22)] unlike in horizontal flows ($U_2'' = mU_1''$ in horizontal flows). Fluid properties have been kept constant in both countercurrent and co-current flow to maintain consistency throughout the work. The viscosity ratio, $m = 1.52$, and density ratio, $r = 1.0335$, are used in this work, which depicts the oil–water system. Previous studies have shown to obtain a larger slip length (of the order of hundreds of micrometer) in a mini-channel flows.[35,37] Chai and Song[71] demonstrated the effects of a higher slip length on stability in a horizontal channel. Larger slip lengths obtained in the experiments allow us to set higher non-dimensional slip coefficient β to study the onset of linear stability in channel flows. The symmetric slip boundary conditions have been used at both walls. The symmetric slip conditions are more relevant at low viscosity ratios. The asymmetric slip boundary condition can be the extension of this work and can be used with higher viscosity ratios.

A. Countercurrent flow

The non-uniqueness of the holdup solutions in an inclined two-layered channel is well identified with the no-slip boundary conditions. Studies on the linear stability analysis of multiple holdup solutions with no-slip boundary conditions have been considered in both the long-wave[18] ($k \ll 1$) and finite wave regimes.[19,20] In this section, we present the long-wave neutral stability plots for countercurrent flows past slippery channel walls. The flow properties and configurations are identical to those adopted in experiments performed by Ullmann *et al.*[17] to demonstrate the multiple holdup solutions in an inclined channel. Subsequently, the neutral stability curves are shown for different inclination angles and channel heights. Two holdup solutions are obtained in a countercurrent flow configuration are identified as LPD mode (light phase dominated) and the HPD mode (heavy phase dominated). In Fig. 7, fluid parameters are set as, $\rho_2 = 916.6$ kg/m^3, $\mu_2 = 2.4 \times 10^{-3}$ Pa s, $H = 1.44 \times 10^{-2}$ m, and $\theta = 10°$. It is shown that with no-slip boundary conditions (shown by thin black lines), a stable region of LPD mode extends to higher values of top layer flow rates, and a stable region for HPD mode extended to higher bottom layer flow rates.[18,20] With wall slip $\beta = 0.05$, a stable LPD mode

TABLE III. Comparison between the present numerical results with the those of Tilley *et al.*,[12] with $m = 100$, $r = 2$, $\theta = 1$ (rad), $We_2 = \frac{(1+n)Re_2^2}{25000}$, $k = \frac{0.001}{(1+n)}$.

n	Re_2	Fr_2	Tilley *et al.*[12]	Present numerics (c_R, c_I)
0.5	5.0742	0.0347 59	(0.296 938 46, 0.000 123 640 57)	(0.296 932 03, 0.000 123 441 586 3)
0.5	11.8	0.0187 97	(0.691 813 21, 0.000 056 307 71)	(0.691 824 344 7, 0.000 056 002 97)
3	26.69	18.236	(6.118 392, 0.001 739 551 8)	(6.118 418 2, 0.001 738 352 47)
3	31.098	2.475 73	(5.215 409, 0.000 966 382)	(5.214 76, 0.000 967 34)

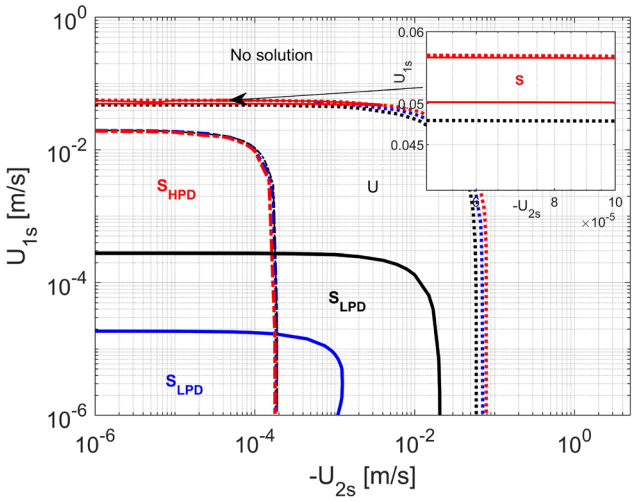

FIG. 7. Long-wave neutral stability plot for countercurrent flow with different slip coefficient β. S_{LPD} corresponds to the stable region in LPD regime; similarly, U corresponds to the unstable region in both solutions. Other parameters are given as $H = 0.0144$ m, $r = 1.0335$, $\theta = 10^{\circ}$, and $m = 1.52$. Black, blue, and red curves indicate $\beta = 0$, 0.05, and 0.1, respectively. (—) corresponds to LPD curves (lower solution in the case of $\beta = 0.1$ case), (– · – ·) corresponds to HPD curves, and (.....) corresponds to flooding curves.

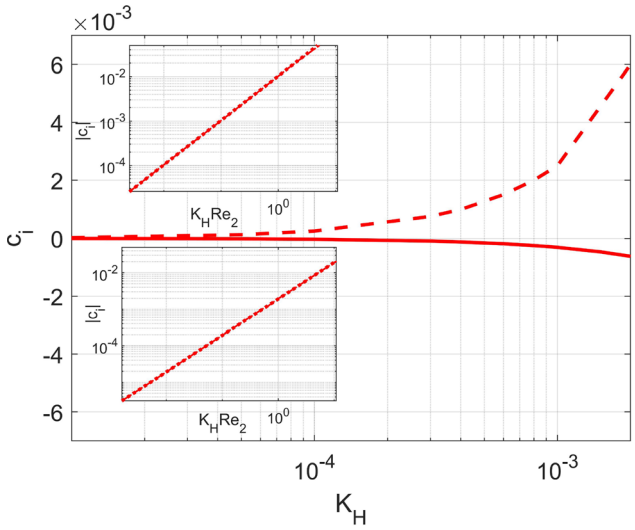

FIG. 8. Imaginary part of the wave speed c_i vs normalized wavenumber plot in lower critical solution for $\beta = 0.1$ in both stable and unstable regions. Stable points represented by $U_{1s} = 0.053$, $U_{2s} = -2 \times 10^{-4}$ m/s, and $h = 0.574$ are shown by a solid line (—). Unstable curves represented by $U_{1s} = 4 \times 10^{-2}$, $U_{2s} = -1 \times 10^{-4}$ m/s, and $h = 0.443$ are shown by a dashed line (– – –). Inset figure in the stable (unstable) region corresponds to the negative (positive) numerical and analytical value of c_i.

shrinks to a lower flow rate range. In this case, it is to be noted that the depth of the top layer h_2 is about 65 times more compared to the depth of the heavy layer. Wall slip induced higher momentum to the bottom and top layers. Therefore, it is expected that the top layer flowing upward is expected to keep a smooth interface only for a limited range of flow rates. Interestingly when $\beta = 0.1$, a small stable region, which belongs to a lower holdup solution, obtained at a relatively higher critical holdup, $h = 0.535$ (shown by a solid red line). The smooth interface is obtained near the center of the channel, unlike when $\beta = 0.05$. The two lower critical holdup solutions bound the stability boundaries. These two critical solutions will meet, and thereby, a stable (and unstable) region is formed for a minimal range of heavy layer flow rates. The upper curve of a lower critical solution is very close to the flooding curve. Though this tiny difference is not visible in a figure, flow in both lower and higher solutions is unstable in the gap between the flooding and upper curves of the critical lower solution. Note that flooding curves are the results of base state calculations embedded in neutral stability diagrams. Beyond the flooding point, flow is expected to change its configuration (to either slug or annular flow) depending upon the flow rates. The flooding curve is shown in the dotted lines with slip boundary conditions.

As similar to the LPD mode, the stable region in the HPD mode is reduced to the lower values of superficial velocities with slippery walls. Therefore, the system's operating range, given in terms of flow rates (or superficial velocities), is decreased with wall slip. It is to be noted that, since h_2 is very low in HPD mode, dimensional slip length in HPD mode is very less in magnitude when compared with the LPD mode. The region where both modes can remain stable reduced to lower values of flow rates when wall slip boundary condition is considered.

Variation of c_i for different normalized wavenumber in lower solution is shown in Fig. 8, in both stable and unstable region with $\beta = 0.1$. A normalized wavenumber is defined as a function of k from the expression, $K_H = k(n+1)$. Note that K_H depends on H, contrary to k which is directly proportional to h_2. For plotting neutral stability diagrams, superficial quantities, such as U_{js}, are used. Therefore, normalized wavenumber becomes an obvious choice for plotting dispersion curves. Two points are selected from a small stable and outside the unstable regions from lower solution (when $\beta = 0.1$) as shown in Fig. 8, which corresponds to decay (and growth) of the imaginary phase speed. Further, a comparison between our numerical calculation of imaginary wave speed (shown by dashed-dotted lines) with our long-wave analytical results (shown by dot lines) is shown (see inset in Figs. 8 and 9). We found a good agreement between our numerical and analytical results in the long-wave region for both lower and higher (HPD) solutions. Comparisons between numerical and analytical results for stable (unstable) point placed in a stable (unstable) region are shown in Figs. 8 and 9.

As mentioned before, velocity and time are scaled by U_I. The negative U_I can be obtained in the HPD mode of countercurrent flow and in upward co-current flow. In HPD mode, imaginary wave speed c_i for different normalized wavenumbers are shown in Fig. 9 in both stable and unstable regions. The growth of an imaginary wave speed is much larger when the slip coefficient is $\beta = 0.1$, indicating that instabilities are enhanced more with higher slip coefficient. At higher wall slip, in stable region, an imaginary wave speed decays more quickly than a higher slip coefficient $\beta = 0.1$.

The variation of amplitudes of critical stream function and its derivative with channel height $y = -n$ to 1 and $\beta = 0.05$, are shown in Fig. 10. It is to be noted that ϕ' and ϕ are proportional to the transverse and stream-wise velocity perturbations u' and v', respectively. The values of critical stream functions and its derivative are normalized by maximum value of stream function in the given domain.

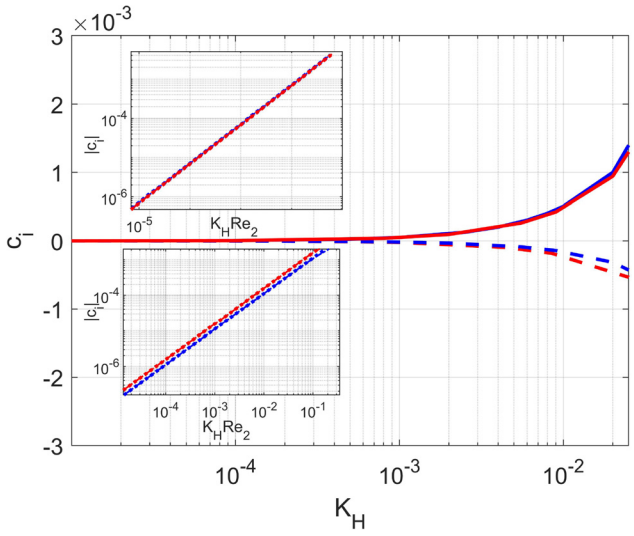

FIG. 9. Imaginary part of the wave speed c_i vs K_H plot in HPD solution. U_l is negative in this case. For stable region, shown by (blue solid line) for $\beta = 0.05$ and (red solid line) for $\beta = 0.1$, we picked $U_{1s} = 10^{-3}$, $U_{2s} = -10^{-4}$ m/s. Holdup $h = 0.957$ when $\beta = 0.05$ and, $h = 0.959$ when $\beta = 0.1$. For an unstable region, shown by (blue dashed line) for $\beta = 0.05$ and (red dashed line) for $\beta = 0.1$. $U_{1s} = 10^{-3}$ and $U_{2s} = -2 \times 10^{-4}$ m/s are same for both slip coefficients $\beta = 0.05$ and $\beta = 0.1$, with holdup $h = 0.946$ and $h = 0.948$, respectively. Inset figure in the stable (unstable) region corresponds to the positive (negative) numerical and analytical values of c_i.

Values of superficial velocities for this figure are taken from the neutral stability curve Fig. 7. The interface is located at $y = 0$ and shown by the dashed line. The magnitude of critical perturbations of the stream function is maximum at the thick light phase of the flow. This indicates the shear mode of instabilities originated at the thick phase, similar to as shown by Barmak *et al.*[20] with no-slip case. The magnitude of critical perturbation of stream function derivative (or stream-wise perturbation velocity) is maximum at the interface. However, a secondary maximum is observed in the light phase. The given results depict the instabilities are originated at the interface and in the bulk of the less viscous fluid due to the long-wave analysis.

With $\beta = 0.1$ (shown in Fig. 11), the maximum value of $|\phi|$ is obtained in the lower heavy phase unlike in the case with $\beta = 0.05$. This is probably expected because both the phases are of approximately equal depths. Though a secondary maximum of critical $|\phi|$ occurs at the top light phase as well. Also, the maximum magnitude of transverse velocity perturbation is originated near the interface. Moreover, the maximum value of critical stream-wise velocity obtained at the interface indicates the dominating interfacial mode of stability with $\beta = 0.1$.

In HPD mode, amplitude of critical perturbation of $|\phi|$ and $|\phi'|$ are shown in Fig. 12. The observations are similar with the $\beta = 0.05$ case in HPD mode, hence not shown here. Secondary maximum near the wall in the cases mentioned above with LPD and HPD may indicate shear instability near the wall. Shear mode of instability is expected near the wall in the thick layers. The magnitude of stream-wise critical perturbations is maximum at the interface in the top light phase. The overall emerging disturbances can be expected at the

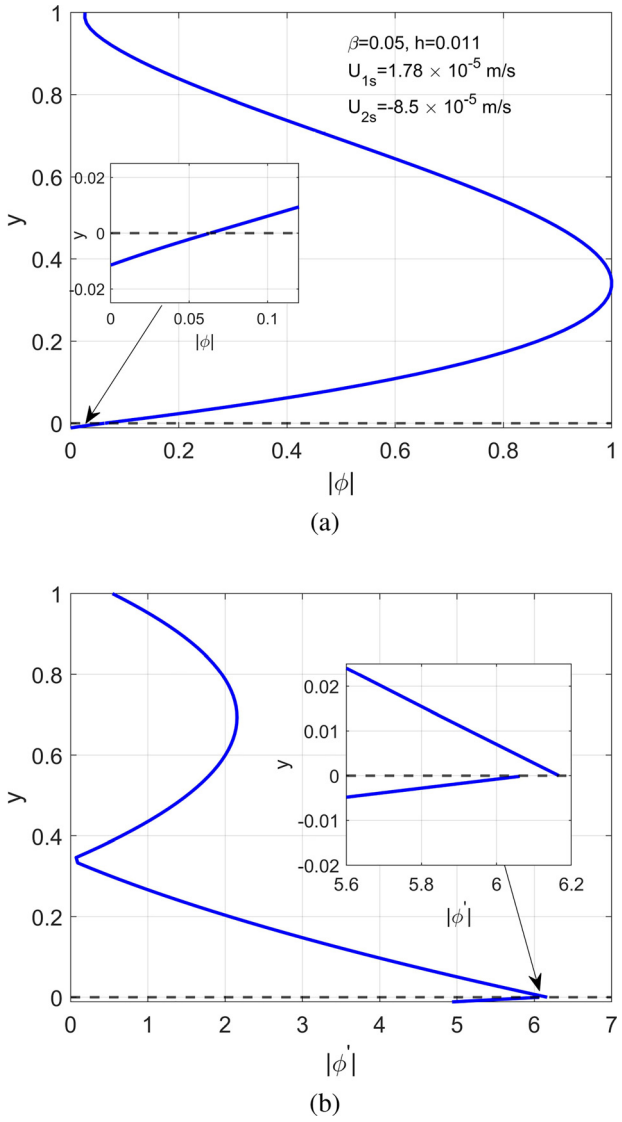

FIG. 10. Amplitudes of critical perturbations of (a) stream functions and (b) its derivative for LPD mode are shown above. Parameters are taken from Fig. 7. Value of $K_H = 10^{-5}$ and $\beta = 0.05$.

interface for the thin phase and near the wall for the thick phase from the long-wave analysis. These observations with slip parameter β are similar to the no-slip case made by Barmak *et al.*[20]

The instability mechanism for the long-wave analysis is well explained by Charru and Hinch[72] by the "thin-layer effect." On moving from stable to unstable region (on higher bottom phase flow rates), the depth of the lower phase decrease. The same conclusion can be made when we fixed a point in the stable LPD region when $\beta = 0$ and then introduces a slip at that point (becomes unstable due to introduction of the slip). As the depth ratio is becoming less, interfacial shear stress can be induced by a thick top phase on the bottom phase. Hence, the thin bottom phase is dragged along with the thick layer

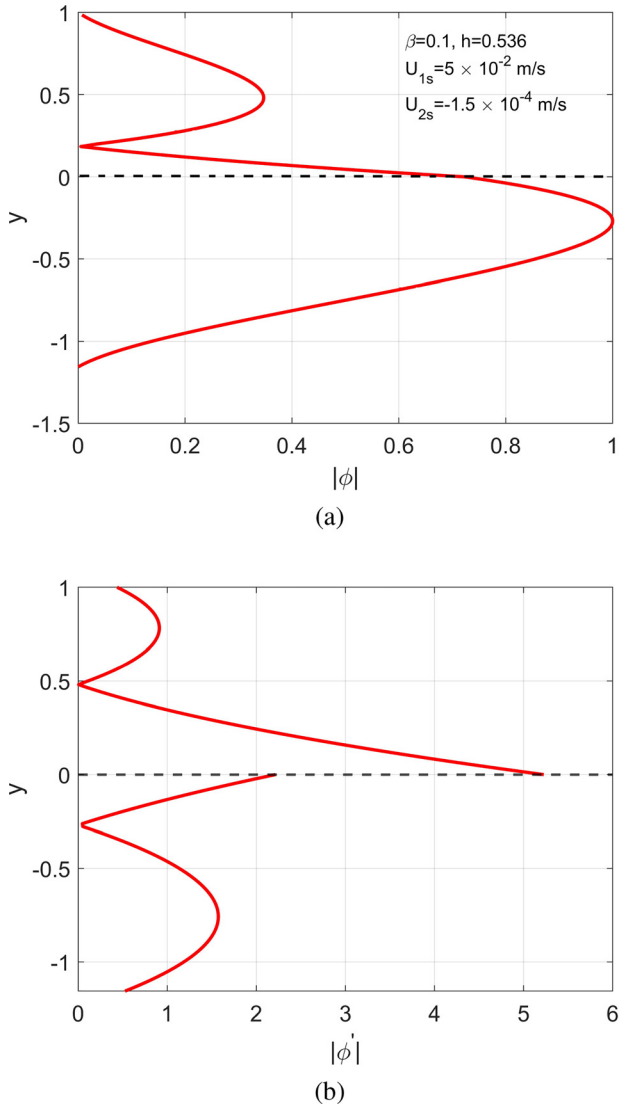

FIG. 11. Amplitudes of critical perturbations of (a) stream functions and (b) its derivative for LPD mode are shown above. Parameters are taken from Fig. 7. Value of $K_H = 10^{-5}$ and $\beta = 0.1$.

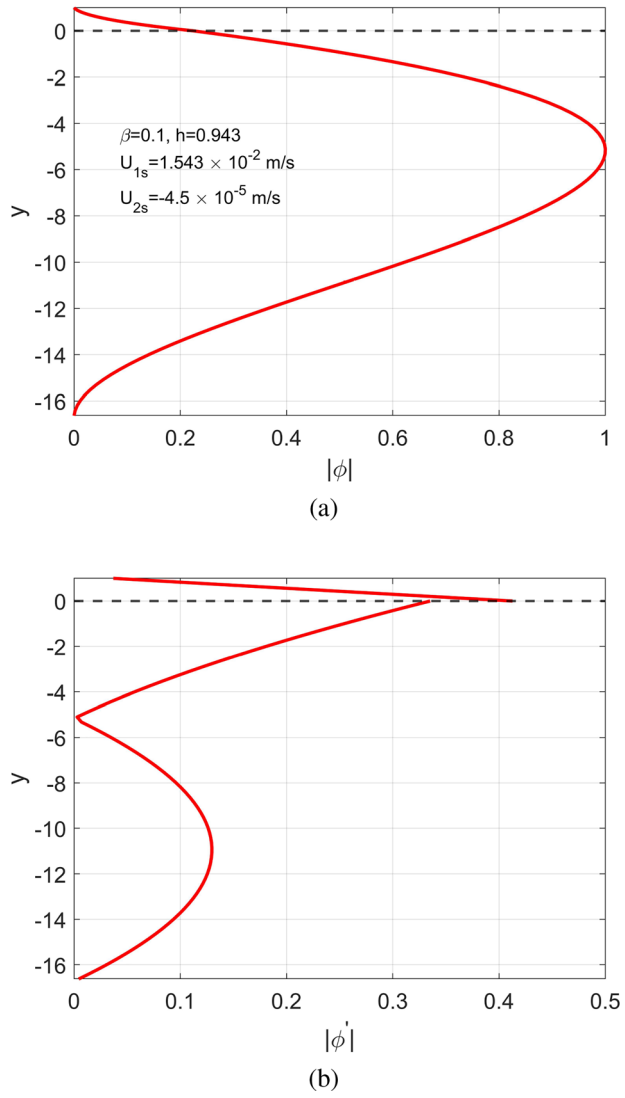

FIG. 12. Amplitudes of critical perturbations of (a) stream functions and (b) its derivative for HPD mode are shown above. Parameters are taken from Fig. 7. Value of $K_H = 10^{-5}$ and $\beta = 0.1$.

and might be responsible for the growing (or decaying) disturbances. In HPD mode, we observed the shear mode of instabilities near the wall and at the interface. It creates the circulation cells of the critical eigenfunctions as shown by Barmak *et al.*[20] The patterns of critical stream function on x and y plane are the same with slip boundary conditions.

In Fig. 7, lower solutions with $\beta = 0.1$ occupies a stable region in an interesting manner. To look if this stable lower solution region is a trend, followed with different parameters, the neutral stability curve is shown when channel height is slightly reduced to 0.01 from 0.0144 m (see Fig. 13). All other flow parameters are kept the same as previously mentioned. Interestingly, the LPD mode is the only stable mode observed with and without slip. The stable region of LPD mode extends to higher flow rates when compared to a previous case with $H = 0.0144$ m. Since no critical HPD mode is observed, it does not violate the non-uniqueness of the holdup solutions in countercurrent flows. It can be interpreted as no smooth interface (stable region) in a two-layered configuration is observed. Hence the wavy (unstable) interface is expected at higher critical holdups. A stable LPD region with slippery walls, is reduced to lower flow rates. With the no-slip condition in LPD mode, a smooth interface is obtained at almost all top layer flow rates until it reaches the flooding point.

It has been shown with an inclination angle $\theta = 26^\circ$ and $\beta = 0$, the stable region for LPD and HPD modes is confined to higher top and bottom layer flow rates, respectively[18] (see Fig. 14). Moreover, a common stable region where both modes can remain stable shrinks

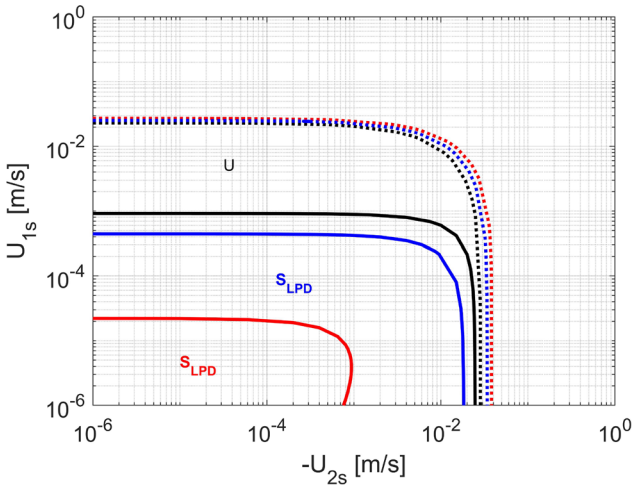

FIG. 13. Long-wave neutral stability plot of countercurrent flow when $H = 0.01$ m. All other parameters are same as specified in Fig. 7. Black, blue, and red curves indicate $\beta = 0$, 0.05, and 0.1, respectively. (—) corresponds to LPD curves, (– · –) corresponds to HPD curves, and (.....) corresponds to flooding curves.

when compared to a $\theta = 10^\circ$ case. The flow became unstable with a slip when the interface is near the bottom wall at all flow rates (LPD mode). Only the stable region in HPD mode is observed with slippery walls. Further, HPD stable zone is reduced to the lower values of superficial velocities when the wall slip boundary condition increases to 0.1. Similar to when $\theta = 10^\circ$ with slip, the effect of wall slip on the stable region in the HPD mode is minimal. It is to be noted that a higher slip coefficient gives extra momentum to both layers. With higher momentum imparted to both layers due to wall slip, the shear stress at the interface is expected to increase and can be responsible for instability with slippery walls.

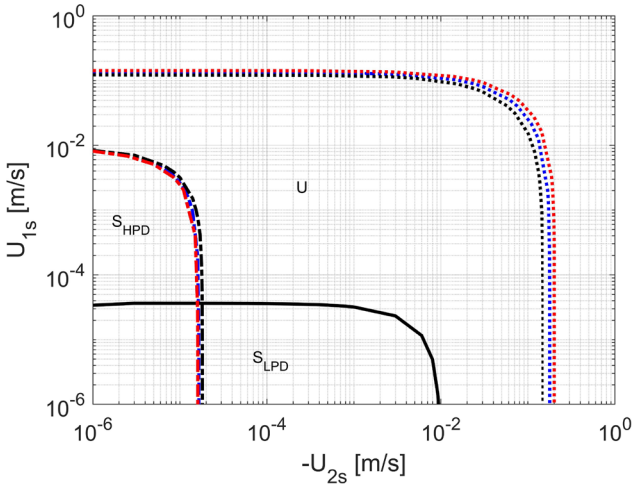

FIG. 14. Long-wave neutral stability plot of countercurrent flow with $\theta = 26^\circ$. All other parameters are same as specified in Fig. 7. Black, blue, and red curves indicate $\beta = 0$, 0.05, and 0.1, respectively. (—) corresponds to LPD curves, (– · –) corresponds to HPD curves, and (.....) corresponds to flooding curves.

In Fig. 15, variation of c_i for different normalized wavenumber is shown for countercurrent flow with $\theta = 26^\circ$ within unstable HPD region. Indeed, the negative values of c_i ($U_I < 0$) are observed. However, as expected with higher slip coefficient $\beta = 0.1$, growth of values of c_i are more in higher wavenumbers. The least unstable c_i are obtained from slip coefficient $\beta = 0.05$. This provides a good validation of higher instability in the HPD mode with slip coefficient $\beta = 0.1$ (see Fig. 14).

To check what happens at larger channel height, the neutral stability curve with channel height $H = 0.03$ m is shown in Fig. 16. The result obtained is almost similar to a case when $\theta = 26^\circ$. With wall slip conditions, flow always remains unstable in LPD mode. In HPD mode, the stable region of flow is reduced to the lesser values of the superficial velocities. When the slip coefficient is $\beta = 0.1$, a stable region is further diminish, to lower superficial velocities than the $\beta = 0.05$ case. When an interface is near the top wall, a portion of a channel is largely occupied by a bottom layer. The unstable region is expected due to the interfacial shear stress able to disturb the flow when the heavy bottom layer is dominated. With higher momentum induced by a slip, flow is expected to remain unstable at higher top layer flow rates than a no-slip case.

It is worth mentioning that physics at the interface plays a crucial role in determining the stability at different interface locations. The range of stable region (in terms of flow rates/superficial velocities) mostly depends on the difference between the two fluids' velocities and the holdup. The slip boundary condition provides extra momentum to both fluid layers at different regimes (LPD and HPD). It alters the relative velocity between two-layers, which changes the interfacial shear stress. In countercurrent flows, we observed destabilizing effects with wall slip in both LPD and HPD mode.

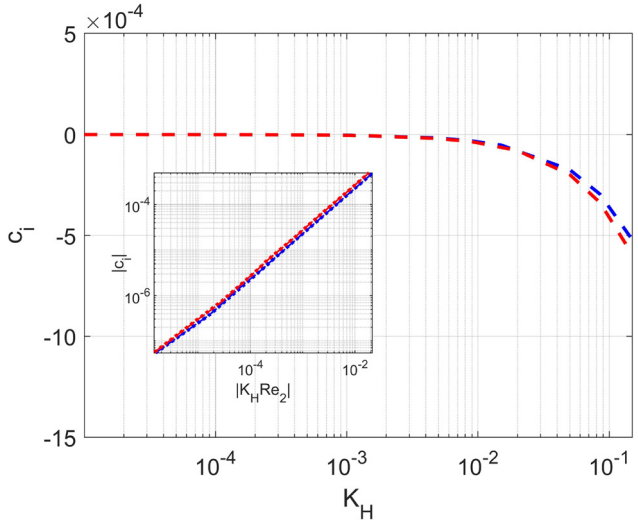

FIG. 15. Imaginary wave speed c_i vs normalized wave-number plot for countercurrent flow with inclination angle $\theta = 26^\circ$ in a unstable HPD region. U_I is negative in this case. $U_{1s} = 10^{-4}$ and $U_{2s} = -2 \times 10^{-5}$ m/s for slip coefficients $\beta = 0.05$ (blue dashed line) and 0.1 (red dashed line), respectively. Inset figure in the stable region corresponds to the positive numerical and analytical values of c_i.

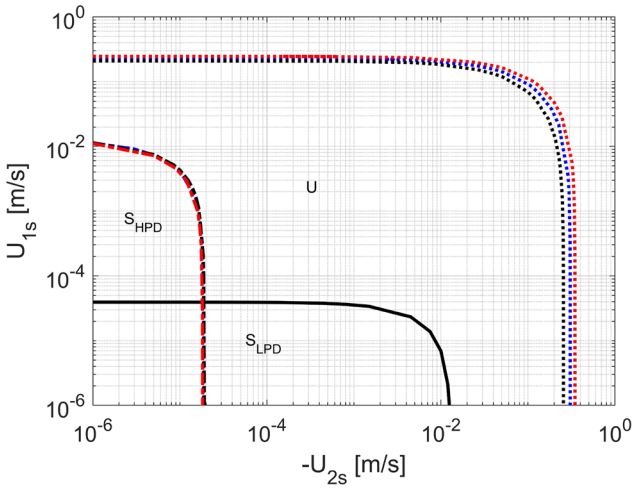

FIG. 16. Long-wave neutral stability plot of countercurrent flow with $H = 0.03$ m. All other parameters are same as specified in Fig. 7. Black, blue, and red curves indicate $\beta = 0$, 0.05, and 0.1, respectively. (—) corresponds to LPD curves, (– · – ·) corresponds to HPD curves, and (.....) corresponds to flooding curves.

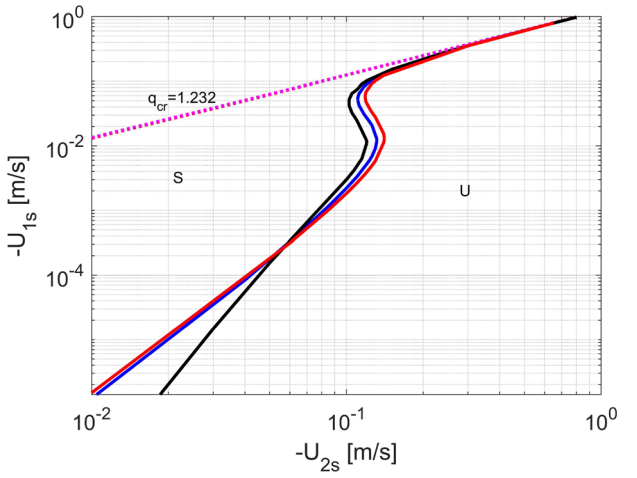

FIG. 17. Long-wave neutral stability curve for upward co-current. $\theta = 0.1°$ and $H = 0.0144$ m. Black, blue, and red curves indicate $\beta = 0$, 0.05, and 0.1, respectively.

An extension of this problem is the falling film down the inclined plane with the slippery wall. Such a situation has already been investigated by Pascal[42] in a porous inclined plane and Samanta *et al.*[47] in a slippery inclined plane using long-wave asymptotic methods. Flows in such cases are mostly unbounded from the topside. Such flow configuration can be attained by keeping the viscosity of top layer zero ($m \to \infty$) with LPD mode appreciated. Depending on the scale, different average momentum equations can be added or modified.

B. Co-current flows

Stability analysis for co-current air–water inclined flow is studied in both long-wave and finite wave regimes at no-slip boundary condition.[18,20] These studies extended to the triple solution region, obtained at a higher gas flow rate in an upward inclined flow and high water flow rates in a downward inclined flow. Necessary care should be taken to get a triple solution region since its complexity in getting multiple holdup solutions increases with the wall slip conditions. It is essential to know the magnitude of Y at different flow rates for a triple solution boundary. Usually, in downward co-current flow ($Y > 0$), triple solution boundary is obtained at the higher magnitude of Y and X^2, which is also demonstrated in Fig. 2. However, in upward co-current flows (when $Y < 0$), the triple solution boundary is expected at lower values of Y and X^2. The parameters and fluid properties are kept the same as mentioned for the countercurrent flows.

The neutral stability curves for co-current liquid–liquid flows in both upward and downward flow configurations are present in a single solution regime with and without wall slip boundary conditions. Here, the single solution is associated with the lower holdup solution in both upward and downward co-current flows.

A neutral stability plot for upward co-current flow, shown in Fig. 17, is analyzed for a slightly inclined channel, $\theta = 0.1°$. Below q_{cr} is the region where the top layer superficial fluid velocity is higher than the bottom layer velocity, and above q_{cr}, the bottom layer superficial fluid velocity is higher comparatively. The stable region above q_{cr} is not affected by a slip boundary condition. The unstable region is obtained at higher values of top layer flow rates below q_{cr}. The wall slip has significant effects on the stability where the relative superficial velocity between the two layers is large. Also, the magnitude of the bottom layer flow rate can influence stability. At lower values of bottom layer flow rates, the stable region is limited to the lower top layer flow rates. This stable region further shrinks to the lower values of top layer flow rates with increasing slip coefficient β. Hence, the flow mostly remains unstable in a higher range of top layer flow rates when the bottom layer flow rate is low. Similarly, when bottom layer flow rates are high, the stable region is enhanced to a larger range of top layer flow rates. Moreover, the wall slip stabilizes the flow at moderate flow rates (at around $U_{2s} \approx -0.15$ m/s). Note that the flow rates are increasing along with holdup h. Therefore, the heavier bottom layer will occupy a larger portion of the channel at higher flow rates.

In Fig. 18, the variation of c_i for different normalized wavenumber is shown for the upward co-current flow. Note that U_I is negative in this case, as previously mentioned. In a stable region (solid lines), c_i is positive at all wavenumbers. Moreover, the decay rate of c_i is increasing with the higher wall slip coefficients. However, this might not be the same with every point in the neutral stability plot shown in Fig. 17, since the slip coefficient can stabilize and destabilize the flow.

The amplitudes of critical $|\phi|$ and $|\phi'|$ for the co-current upward flow are shown in Fig. 19. The maximum amplitude of critical transverse velocity is obtained in the light thick upper layer and at the interface. At the interface, a sudden increase in the critical $|\phi|$ may indicate that instabilities are triggered by interfacial mode as well. The maximum amplitude for critical stream-wise perturbation velocity is obtained at the interface.

In Fig. 20, the neutral stability curve for downward liquid–liquid flow is shown in a single solution region. When the slip coefficient is $\beta = 0.05$, the flow is unstable at lower flow rates than the no-slip case. At higher flow rates, a neutral stability curve with $\beta = 0.05$ is almost following the curve with the no-slip case with small enhancement in the stable region. When a higher slip coefficient $\beta = 0.1$ is considered,

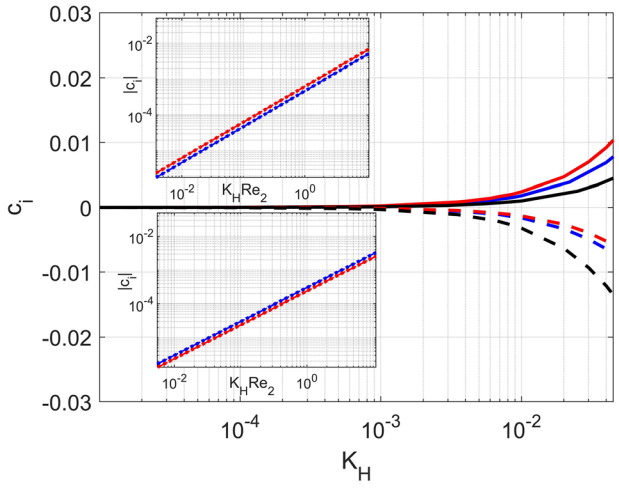

FIG. 18. Imaginary part of wave speed c_i vs normalized wavenumber from upward co-current plot. U_l is negative in this case. Points picked up from Fig. 17 stable region are $U_{1s} = -0.01$ and $U_{2s} = -0.1$ m/s indicated by (—) for $\beta = 0$, (blue solid line) for $\beta = 0.05$ and (red solid line) for $\beta = 0.1$. Points from unstable region are $U_{1s} = -0.01$ and $U_{2s} = -0.18$ m/s indicated by (– – –) for $\beta = 0$, (blue dashed line) for $\beta = 0.05$ and (red dashed line) for $\beta = 0.1$. Inset figure in the stable (unstable) region corresponds to the positive (negative) numerical and analytical values of c_i.

unlike in upward co-current flow, the stable region is enhanced for all flow rates compared to the no-slip boundary condition and $\beta = 0.05$. Unlike in a previous case (upward flow), the wall slip does not significantly affect the stability when both layers' relative velocity is high. The wall slip also has negligible effects on the stability above the q_{cr} region.

The variation of c_i for different normalized wavenumber is shown in Fig. 21 for the downward co-current flow. The stable c_i in all wavenumbers K_H is obtained, which decays further at higher wavenumbers. However, in an unstable region, the imaginary wave speed shows a similar behavior as in previously mentioned cases with slip conditions.

The amplitudes of critical $|\phi|$ and $|\phi'|$ for the co-current downward flow are shown in Fig. 22. The maximum amplitude of critical transverse velocity perturbations is obtained at the interface. The critical stream-wise velocity perturbations are maximum at the interface at the bottom phase side. In the co-current downward flow, instabilities are likely to be of interfacial mode.

The triple solution region in the co-current flow is rather complicated to obtain. It is a bounded region where all three solutions can exist. It is reported that all three solutions can become stable within the triple solution boundary region obtained in air–water co-current inclined channel flows.[18,20] In liquid–liquid co-current flows, triple solution boundaries are acquired at lower top layer flow rates for both upward and downward flows, unlike in the case of air–water inclined flow (see Fig. 23). In upward co-current flows, the boundary of a triple solution is obtained at very less bottom layer superficial velocity (at around $U_{1s} = 10^{-8}$ m/s) and a minimal range of top layer superficial velocities U_{2s}. Therefore, only the triple solution boundary region for downward co-current inclined flows is demonstrated below. The triple solution boundary region expands with higher slip coefficients to higher heavy bottom layer flow rates. Additional critical holdup

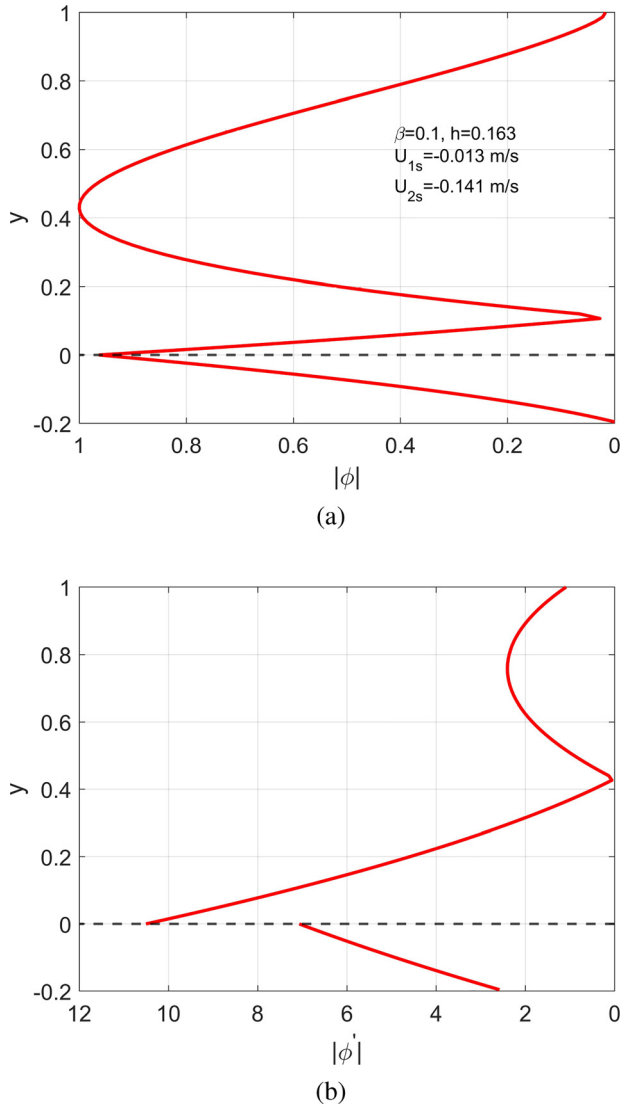

FIG. 19. Amplitudes of critical perturbations of (a) stream functions and (b) its derivative for upward co-current flows are shown above. Parameters are taken from Fig. 17. Value of $K_H = 10^{-5}$ and $\beta = 0.1$.

solutions are obtained inside triple solution boundaries, which are not shown in this figure. These additional critical bottom phase superficial velocities belong to the middle and higher holdups.

VI. CONCLUSION

Multiple holdups in an inclined channel flow are well-established facts. The stability of these holdup solutions depends on the flow properties and parameters. One such parameter is the slip boundary condition. In this paper, we have performed the linear stability analysis in the countercurrent and co-current flow, considering their multiple holdup solutions obtained in the slippery inclined channel. We derived the base state for a two-layered inclined flow and studied non-unique holdup solutions with a wall slip boundary condition. When the

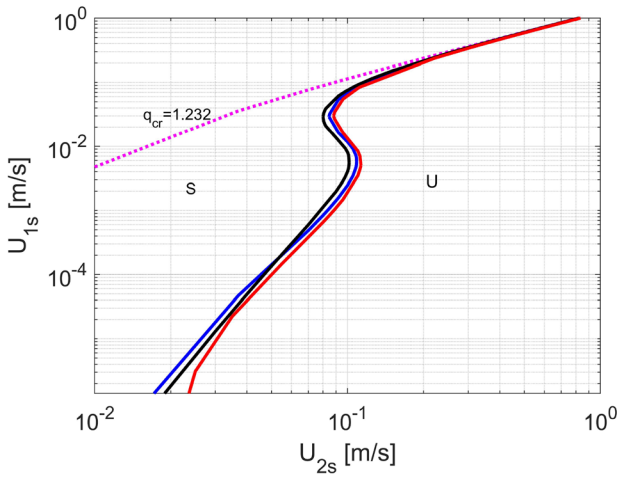

FIG. 20. Long-wave neutral stability curve for downward co-current. $\theta = 1^\circ$ and $H = 0.0144$ m. Black, blue, and red curves indicate $\beta = 0$, 0.05, and 0.1, respectively.

interface is near the bottom wall (for lower holdup solutions), the base state is obtained at the high flow rate ratio. When the interface near the top wall, wall slip barely affects the flow rate ratio. However, the base states are obtained closer to the top wall (higher holdup value) than the no-slip boundary condition.

The linear stability analysis is carried out by solving the Orr–Sommerfeld equations for both layers. The asymptotic analysis is carried out by taking wavenumber approaching zero (in a long-wave limit), and eigenvalues are obtained until the first order.

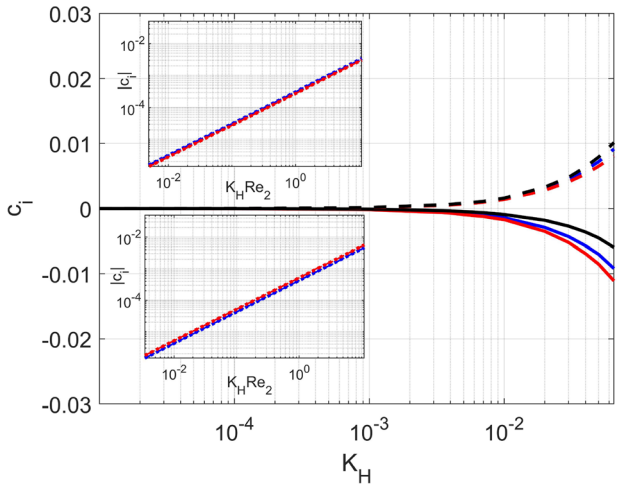

FIG. 21. Imaginary part of wave speed c_i vs normalized wavenumber for downward co-current flow. Interfacial velocity is positive for this case. Points picked up from Fig. 20 stable region are $U_{1s} = 10^{-2}$ and $U_{2s} = 8 \times 10^{-2}$ m/s indicated by (—) for $\beta = 0$, (blue solid line) for $\beta = 0.05$ and (red solid line) for $\beta = 0.1$. Points from unstable region are $U_{1s} = 10^{-2}$ and $U_{2s} = 0.15$ m/s indicated by (– – –) for $\beta = 0$, (blue dashed line) for $\beta = 0.05$ and (red dashed line) for $\beta = 0.1$. Inset figure in the stable (unstable) region corresponds to the negative (positive) numerical and analytical values of c_i.

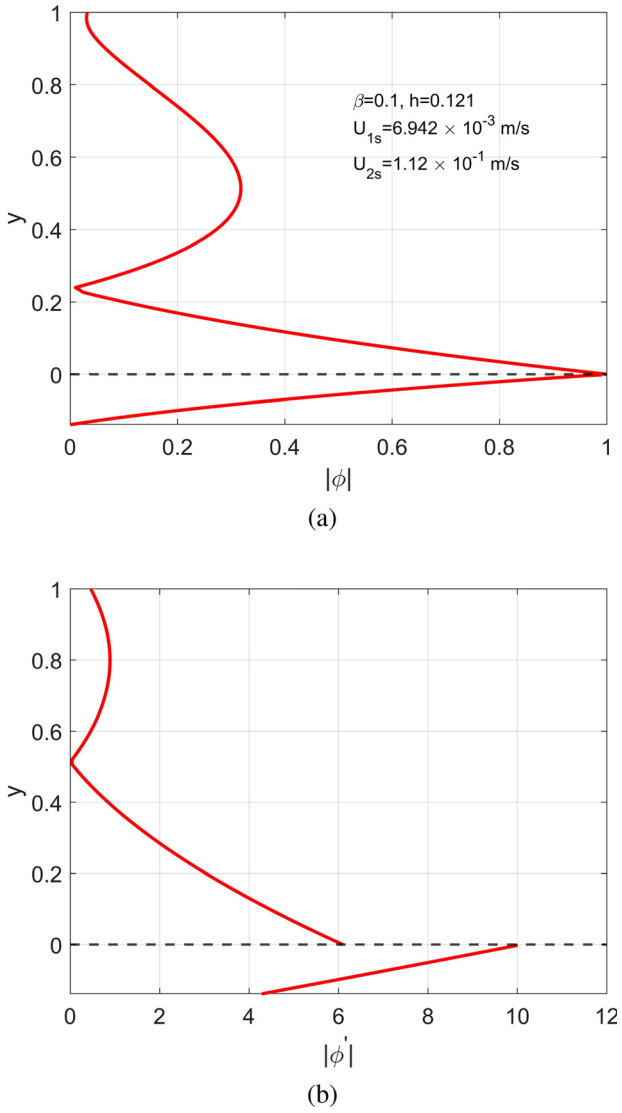

FIG. 22. Amplitudes of critical perturbations of (a) stream functions and (b) its derivative for downward co-current flows are shown above. Parameters are taken from Fig. 20. Value of $K_H = 10^{-5}$ and $\beta = 0.1$.

Analytical results are validated numerically by using Chebyshev collocation spectral method in MATLAB.

The results are presented in the form of neutral stability plots with a larger magnitude of non-dimensional wall slip coefficients $\beta = 0.05$ and 0.1 and then compared with the no-slip case.[18] In the inclined channel flows, we found that the interface's location and wall slip played a crucial role in determining the operational range in terms of superficial velocities (or flow rates) where a smooth interface can be observed. The multiple base states allow the different locations of an interface at each solution distinguished as the lower and higher holdup in countercurrent flows (middle holdup in co-current flow). We found that LPD mode is sensitive to stability in countercurrent flows when slip boundary condition is introduced. The interface near the bottom

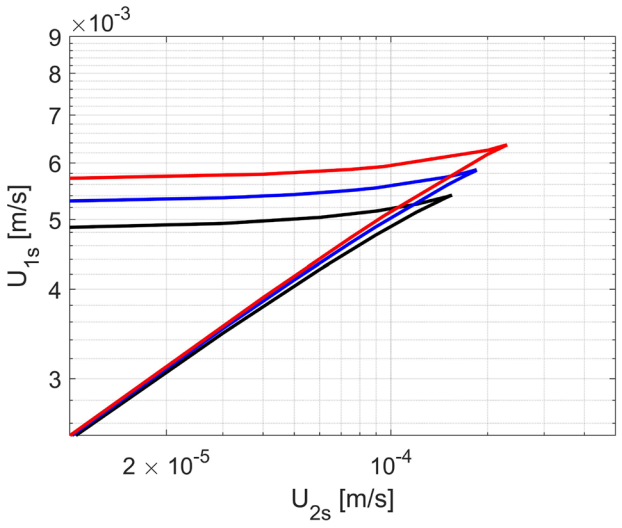

FIG. 23. Triple solution boundary region for downward liquid–liquid co-current inclined channel flows. Black curve indicates no slip condition, blue curve indicates slip with $\beta = 0.05$, and red curve indicates slip with $\beta = 0.1$.

wall is stable for only a limited flow rate with wall slip coefficients $\beta = 0.05$. At higher wall slip coefficients, the stable region is further reduced to an even lower range of flow rates or completely disappeared. Similarly, in HPD mode, the stable regions reduced to lower flow rates when slip is considered. At a higher inclination angle and channel height, the interface is stable only if it is placed near a top wall (with and without wall slip). Amplitudes of the critical stream functions are the maximum at the bulk thick phase in HPD mode. A similar argument is shown by Barmak *et al.*[20] with the no-slip case. The instabilities in LPD mode can be of interfacial mode, and the "thin-layer effect" might be the possible explanation.[72] As flow transitions from stable to unstable region and from no-slip to slip boundary conditions take place, the depth of the lower thin layer decreases. The thick top phase induces the interfacial shear stress at the lower thin phase and produces a drag which can be responsible for the growth of the disturbance. Moreover, the critical eigenfunction is maximum near the interface, and its derivative is maximum at the interface, indicating the interfacial mode of instability in LPD mode.

We present the neutral stability plots for liquid–liquid inclined co-current flows. The wall slip stabilizes and destabilizes the co-current flow, which depends on the superficial velocities and holdups. In the co-current upward flows, the wall slip condition destabilizes the flows to lower layer flow rates at lower holdups. However, at higher holdups, the stability is obtained at higher flow rates U_{2s} relatively to no-slip boundary conditions. The effect of wall slip on instability depends on the bottom layer flow rate (U_{1s}). In downward flows, the wall slip coefficient $\beta = 0.1$ extends the stability boundaries at all critical holdups. However, the stable region occupies the lower range of top layer flow rates with wall slip coefficients $\beta = 0.05$. Most critical eigenfunctions perturbations are obtained near the interface, which indicates the interfacial mode of instabilities that arises in the co-current flows. Moreover, the instabilities' mechanism can be understood by the "thin layer effect" similar to the LPD mode in the countercurrent flows. Moreover, unlike the air–water case, the triple solution is obtained at lower light layer flow rates in liquid–liquid co-current flow. With the wall slip boundary conditions, this boundary region expands to higher flow rates.

It is necessary to know the operating range of flow rates or superficial velocities where a smooth interface is obtained in different holdup solutions. We expect that LPD mode is more closely dependent on the flow properties along with several flow parameters. Therefore, one can observe several interesting stable regions to span over different ranges of low rates considering various fluids with or without wall slip conditions. A triple solution region in co-current liquid–liquid flows and the stability of holdup solutions inside it for different flow rates is still an unexplored area.

SUPPLEMENTARY MATERIAL

See the supplementary material for the coefficients given in Eqs. (28), (29), and (33) obtained in the zeroth and first order from the long-wave analysis.

DATA AVAILABILITY

The data that support the findings of this study are available within the article and its supplementary material.

REFERENCES

[1]K. M. Konsoer and B. L. Rhoads, "Spatial-temporal structure of mixing interface turbulence at two large river confluences," Environ. Fluid Mech. **14**, 1043–1070 (2014).
[2]G. Ponetti, N. J. Balmforth, and T. S. Eaves, "Instabilities in a staircase stratified shear flow," Geophys. Astrophys. Fluid Dyn. **112**, 1–19 (2018).
[3]J. R. Carpenter, E. W. Tedford, E. Heifetz, and G. A. Lawrence, "Instability in stratified shear flow: Review of a physical interpretation based on interacting waves," Appl. Mech. Rev. **64**, 060801 (2011).
[4]R. Govindarajan and K. C. Sahu, "Instabilities in viscosity-stratified flow," Annu. Rev. Fluid Mech. **46**, 331–353 (2014).
[5]C.-S. Yih, "Instability due to viscosity stratification," J. Fluid Mech. **27**, 337–352 (1967).
[6]A. P. Hooper and W. G. C. Boyd, "Shear-flow instability at the interface between two viscous fluids," J. Fluid Mech. **128**, 507–528 (1983).
[7]S. G. Yiantsios and B. G. Higgins, "Linear stability of plane Poiseuille flow of two superposed fluids," Phys. Fluids **31**, 3225–3238 (1988).
[8]A. Kaffel and A. Riaz, "Eigenspectra and mode coalescence of temporal instability in two-phase channel flow," Phys. Fluids **27**, 042101 (2015).
[9]C.-S. Yih, "Stability of liquid flow down an inclined plane," Phys. Fluids **6**, 321–334 (1963).
[10]S. Kalliadasis, C. Ruyer-Quil, B. Scheid, and M. Velarde, *Falling Liquid Films* (Springer, 2012).
[11]M. K. Smith, "The long-wave instability in heated or cooled inclined liquid layers," J. Fluid Mech. **219**, 337–360 (1990).
[12]B. S. Tilley, S. H. Davis, and S. G. Bankoff, "Linear stability theory of two-layer fluid flow in an inclined channel," Phys. Fluids **6**, 3906–3922 (1994).
[13]B. Vempati, A. Oztekin, and S. Neti, "Stability of two-layered fluid flows in an inclined channel," Acta Mech. **209**, 187–199 (2010).
[14]Y. Y. Trifonov, "Calculation of linear stability of a stratified gas–liquid flow in an inclined plane channel," J. Appl. Mech. Tech. Phys. **59**, 52–60 (2018).
[15]M. J. Landman, "Non-unique holdup and pressure drop in two-phase stratified inclined pipe flow," Int. J. Multiphase Flow **17**, 377–394 (1991).
[16]D. Barnea and Y. Taitel, "Structural and interfacial stability of multiple solutions for stratified flow," Int. J. Multiphase Flow **18**, 821–830 (1992).
[17]A. Ullmann, M. Zamir, Z. Ludmer, and N. Brauner, "Stratified laminar countercurrent flow of two liquid phases in inclined tubes," Int. J. Multiphase Flow **29**, 1583–1604 (2003).
[18]R. Kushnir, V. Segal, A. Ullmann, and N. Brauner, "Inclined two-layered stratified channel flows: Long wave stability analysis of multiple solution regions," Int. J. Multiphase Flow **62**, 17–29 (2014).

[19]I. Barmak, A. Gelfgat, H. Vitoshkin, A. Ullmann, and N. Brauner, "Stability of stratified two-phase flows in horizontal channels," Phys. Fluids **28**, 044101 (2016).
[20]I. Barmak, A. Y. Gelfgat, A. Ullmann, and N. Brauner, "Stability of stratified two-phase flows in inclined channels," Phys. Fluids **28**, 084101 (2016).
[21]D. Thibault, J.-M. Munoz, and A. Liné, "Multiple holdup solutions in laminar stratified flow in inclined channels," Int. J. Multiphase Flow **73**, 275–288 (2015).
[22]D. Picchi, I. Barmak, A. Ullmann, and N. Brauner, "Stability of stratified two-phase channel flows of Newtonian/non-Newtonian shear-thinning fluids," Int. J. Multiphase Flow **99**, 111–131 (2018).
[23]E. Lauga and C. Cossu, "A note on the stability of slip channel flows," Phys. Fluids **17**, 088106 (2005).
[24]D. C. Tretheway and C. D. Meinhart, "Apparent fluid slip at hydrophobic microchannel walls," Phys. Fluids **14**, L9–L12 (2002).
[25]Y. Zhu and S. Granick, "Limits of the hydrodynamic no-slip boundary condition," Phys. Rev. Lett. **88**, 106102 (2002).
[26]C. L. M. H. Navier, "Mémoire sur les lois du mouvement des fluides," Mém. Acad. R. Sci. Inst. Fr. **6**, 389–440 (1823).
[27]M. J. Miksis and S. H. Davis, "Slip over rough and coated surfaces," J. Fluid Mech. **273**, 125–139 (1994).
[28]K. Watanabe, Yanuar, and H. Mizunuma, "Slip of Netwonian fluids at slid boundary," JSME Int. J., Ser. B **41**, 525–529 (1998).
[29]K. Watanabe, Y. Udagawa, and H. Udagawa, "Drag reduction of Newtonian fluid in a circular pipe with a highly water-repellent wall," J. Fluid Mech. **381**, 225–238 (1999).
[30]K. Watanabe and H. Udagawa, "Drag reduction of non-Newtonian fluids in a circular pipe with a highly water-repellent wall," AIChE J. **47**, 256–262 (2001).
[31]R. Pit, H. Hervet, and L. Léger, "Direct experimental evidence of slip in hexadecane: Solid interfaces," Phys. Rev. Lett. **85**, 980–983 (2000).
[32]E. Ruckenstein and P. Rajora, "On the no-slip boundary condition of hydrodynamics," J. Colloid Interface Sci. **96**, 488–491 (1983).
[33]N. V. Churaev, V. D. Sobolev, and A. N. Somov, "Slippage of liquids over lyophobic solid surfaces," J. Colloid Interface Sci. **97**, 574–581 (1984).
[34]Y. Ichikawa, K. Yamamoto, M. Yamamoto, and M. Motosuke, "Near-hydrophobic-surface flow measurement by micro-3D PTV for evaluation of drag reduction," Phys. Fluids **29**, 092005 (2017).
[35]K. B. Migler, H. Hervet, and L. Leger, "Slip transition of a polymer melt under shear stress," Phys. Rev. Lett. **70**, 287–290 (1993).
[36]V. Mhetar and L. Archer, "Slip in entangled polymer melts. 1. General features," Macromolecules **31**, 8607–8616 (1998).
[37]C. Lee, C.-H. Choi, and C.-J. Kim, "Structured surfaces for a giant liquid slip," Phys. Rev. Lett. **101**, 064501 (2008).
[38]R. S. Voronov, D. V. Papavassiliou, and L. L. Lee, "Review of fluid slip over superhydrophobic surfaces and its dependence on the contact angle," Ind. Eng. Chem. Res. **47**, 2455–2477 (2008).
[39]B. Liu and Y. Zhang, "A numerical study on the natural transition locations in the flat-plate boundary layers on superhydrophobic surfaces," Phys. Fluids **32**, 124103 (2020).
[40]M. A. Samaha and M. Gad-el Hak, "Slippery surfaces: A decade of progress," Phys. Fluids **33**, 071301 (2021).
[41]G. Beavers and D. Joseph, "Boundary conditions at a naturally permeable wall," J. Fluid Mech. **30**, 197–207 (1967).
[42]J. P. Pascal, "Linear stability of fluid flow down a porous inclined plane," J. Phys. D: Appl. Phys. **32**, 417–422 (1999).
[43]S. Ghosh and R. Usha, "Stability of viscosity stratified flows down an incline: Role of miscibility and wall slip," Phys. Fluids **28**, 104101 (2016).
[44]R. Govindarajan, "Effect of miscibility on the linear instability of two-fluid channel flow," Int. J. Multiphase Flow **30**, 1177–1192 (2004).
[45]C.-J. Gan and Z.-N. Wu, "Short-wave instability due to wall slip and numerical observation of wall-slip instability for microchannel flows," J. Fluid Mech. **550**, 289–306 (2006).
[46]K. C. Sahu and O. K. Matar, "Three-dimensional linear instability in pressure-driven two-layer channel flow of a Newtonian and a Herschel–Bulkley fluid," Phys. Fluids **22**, 112103 (2010).
[47]A. Samanta, C. Ruyer-Quil, and B. Goyeau, "A falling film down a slippery inclined plane," J. Fluid Mech. **684**, 353–383 (2011).
[48]S. Ghosh, R. Usha, and K. C. Sahu, "Double-diffusive two-fluid flow in a slippery channel: A linear stability analysis," Phys. Fluids **26**, 127101 (2014).
[49]S. Ghosh, R. Usha, and K. C. Sahu, "Linear stability analysis of miscible two-fluid flow in a channel with velocity slip at the walls," Phys. Fluids **26**, 014107 (2014).
[50]G. Chattopadhyay and R. Usha, "On the Yih–Marangoni instability of a two-phase plane Poiseuille flow in a hydrophobic channel," Chem. Eng. Sci. **145**, 214–232 (2016).
[51]E. Ellaban, J. P. Pascal, and S. J. D. D'Alessio, "Instability of a binary liquid film flowing down a slippery heated plate," Phys. Fluids **29**, 092105 (2017).
[52]T. Min and J. Kim, "Effects of hydrophobic surface on stability and transition," Phys. Fluids **17**, 108106 (2005).
[53]A. Samanta, "Non-modal stability analysis in viscous fluid flows with slippery walls," Phys. Fluids **32**, 064105 (2020).
[54]G. Chattopadhyay, K. C. Sahu, and R. Usha, "Spatio-temporal instability of two superposed fluids in a channel with boundary slip," Int. J. Multiphase Flow **113**, 264–278 (2019).
[55]G. Chattopadhyay, R. Usha, and K. C. Sahu, "Core-annular miscible two-fluid flow in a slippery pipe: A stability analysis," Phys. Fluids **29**, 097106 (2017).
[56]S. Ghosh, R. Usha, and K. C. Sahu, "Absolute and convective instabilities in double-diffusive two-fluid flow in a slippery channel," Chem. Eng. Sci. **134**, 1–11 (2015).
[57]K. K. Srinivas and S. S. Diwan, "Energy budget analysis and neutral curve characteristics for the linear instability of Couette–Poiseuille flow," Phys. Fluids **33**, 034102 (2021).
[58]S. Chakraborty, T. W.-H. Sheu, and S. Ghosh, "Dynamics and stability of a power-law film flowing down a slippery slope," Phys. Fluids **31**, 013102 (2019).
[59]V. Ramakrishnan, R. Mushthaq, A. Roy, and S. Vengadesan, "Stability of two-layer flow past slippery surfaces. Part 1: Horizontal channels," Phys. Fluids (to be published).
[60]D. Lumma, A. Best, A. Gansen, F. Feuillebois, J. O. Rädler, and O. I. Vinogradova, "Flow profile near a wall measured by double-focus fluorescence cross-correlation," Phys. Rev. E **67**, 056313 (2003).
[61]U. Boehnke, T. Remmler, H. Motschmann, S. Wurlitzer, J. Hauwede, and T. Fischer, "Partial air wetting on solvophobic surfaces in polar liquids," J. Colloid Interface Sci. **211**, 243–251 (1999).
[62]E. Lauga, M. P. Brenner, and H. A. Stone, "Microfluidics: The no-slip boundary condition," arXiv:cond-mat/0501557 (2005).
[63]K. A. Nair and A. Sameen, "Experimental study of slip flow at the fluid-porous interface in a boundary layer flow," Procedia IUTAM **15**, 293–299 (2015).
[64]K. A. Nair, A. Sameen, and S. A. Lal, "Passive boundary layer flow control using porous lamination," Transp. Porous Media **124**, 533–551 (2018).
[65]J. Lu, H. K. Jang, S. B. Lee, and W. R. Hwang, "Characterization on the anisotropic slip for flows over unidirectional fibrous porous media for advanced composites manufacturing," Composites, Part A **100**, 9–19 (2017).
[66]Y. Taitel and A. E. Dukler, "A model for predicting flow regime transitions in horizontal and near horizontal gas–liquid flow," AIChE J. **22**, 47–55 (1976).
[67]T. I. Hesla, F. R. Pranckh, and L. Preziosi, "Squire's theorem for two stratified fluids," Phys. Fluids **29**, 2808–2811 (1986).
[68]I. Barmak, A. Y. Gelfgat, A. Ullmann, and N. Brauner, "On the squire's transformation for stratified two-phase flows in inclined channels," Int. J. Multiphase Flow **88**, 142–151 (2017).
[69]K. C. Sahu and R. Govindarajan, "Linear stability analysis and direct numerical simulation of two-layer channel flow," J. Fluid Mech. **798**, 889–909 (2016).
[70]L. N. Trefethen, *Spectral Methods in MATLAB* (SIAM, 2000), Vol. 10.
[71]C. Chai and B. Song, "Stability of slip channel flow revisited," Phys. Fluids **31**, 084105 (2019).
[72]F. Charru and E. J. Hinch, "'Phase diagram' of interfacial instabilities in a two-layer Couette flow and mechanism of the long-wave instability," J. Fluid Mech. **414**, 195–223 (2000).